Forest Breeze–Cold Pool Interactions Drive Convective Organization over Heterogeneous Vegetation

BENJAMIN D. ASCHER,[a] STEPHEN M. SALEEBY,[a] PETER J. MARINESCU,[a] AND SUSAN C. VAN DEN HEEVER[a]

[a] *Department of Atmospheric Science, Colorado State University, Fort Collins, Colorado*

(Manuscript received 7 May 2024, in final form 5 September 2024, accepted 1 November 2024)

ABSTRACT: Heterogeneous landscapes can influence the development of convection through the generation of thermally driven mesoscale circulations. To assess the impacts of these circulations and their interaction with sea breezes, we simulated convection in an idealized coastal environment using the Regional Atmospheric Modeling System (RAMS). We compared simulations with striped patterns of surface vegetation to those of uniform vegetation to identify the importance of vegetation heterogeneity in impacting convective development. Under dry soil conditions representative of those during the Tracking Aerosol Convection Interactions Experiment (TRACER) and Experiment of Sea Breeze Convection, Aerosols, Precipitation, and Environment (ESCAPE) campaigns in June 2022, we found that these vegetation-induced circulations, referred to in the literature as "forest breezes," are more important than the sea breeze in determining the location of convection initiation. Convection and precipitation are also found to be favored over forests and suppressed over pasture and suburban landscapes as a result of greater surface sensible heat flux over the forest. Our findings also indicate that forest breezes are important for initiating convection along the boundaries of the forest, but that cold pools may play a key role in propagating the forest breezes toward the center of the forest stripe. In our simulations, the collisions of these breezes in the center of the forest stripe lead to uplift and strong convection there; however, a different width of the forest stripe would alter when the forest breezes collide or whether they collide at all. The presence of these cold pools may therefore impact the "ideal stripe width," the width of each vegetation stripe which maximizes domain-wide precipitation.

KEYWORDS: Mesoscale processes; Vegetation-atmosphere interactions; Atmosphere-land interaction; Cold pools; Convective storms; Cloud resolving models

1. Introduction

The location and timing of convective storms, as well as their impacts and hazards, are highly dependent on the surrounding distribution of temperature, wind, and humidity, referred to in this paper as the "convective environment" (Derbyshire et al. 2004; Rapp et al. 2011; Weisman and Klemp 1984). This convective environment is affected by the development of the planetary boundary layer (PBL) throughout the day. The development of the PBL is itself affected by land surface properties, as different land surfaces absorb different amounts of solar radiation, impart different latent and sensible heat fluxes to the overlying atmosphere, and lead to changes in atmospheric stability, moisture, and wind speed and direction (Anthes 1984; Ookouchi et al. 1984; Drager et al. 2022; Segal et al. 1995). For example, a desert with a smooth, highly reflective surface and no transpiring vegetation will likely have lower energy fluxes to the atmosphere and a larger Bowen ratio than a lush tropical jungle with tall, dark-leaved trees and large amounts of transpiration.

Several studies have examined the relationship between land surface properties and the occurrence of cloud formation and precipitation. The 1D numerical modeling experiments over uniform terrain have found that lower Bowen ratios result in more favorable conditions for deep convection over both bare soil and vegetated surfaces, while 3D numerical modeling experiments have reported an increase in precipitation over more moist bare soils, but a nonmonotonic relationship between surface Bowen ratios and precipitation over vegetated surfaces (Drager et al. 2022; Segal et al. 1995).

It is important to note that, in landscapes with heterogeneous land cover, the development of convection is strongly affected by the gradients in land surface properties between "patches" of different land-cover types. For example, a storm which forms over a square of pasture in a checkerboard landscape of pasture and broadleaf forest will behave differently than a storm which forms over a uniform pasture landscape (Anthes 1984; Bou-Zeid et al. 2020; Rieck et al. 2014; Wang et al. 2011). The reason for this is that gradients in land cover produce mesoscale circulations at the boundary of different land-cover types. These mesoscale circulations arise as different land-cover properties lead to differences in heat, vapor, and momentum fluxes to the atmosphere, which in turn leads to gradients in the convective environment (Anthes 1984; Ookouchi et al. 1984; Giorgi and Avissar 1997). Such gradients then induce baroclinic circulations which can help

Denotes content that is immediately available upon publication as open access.

Supplemental information related to this paper is available at the Journals Online website: https://doi.org/10.1175/JAS-D-24-0084.s1.

Ascher's current affiliation: Meteorological Institute Munich, Ludwig Maximilian University, Munich, Germany.

Corresponding author: Benjamin D. Ascher, ben.ascher@lmu.de

DOI: 10.1175/JAS-D-24-0084.1

initiate convection in certain areas and suppress it in others. Although mesoscale circulations induced by vegetation heterogeneity have been described in previous literature, there has not been a consistent name for these circulations (Anthes 1984; Ookouchi et al. 1984; Esau and Lyons 2002; Lee and Kimura 2001; Patton et al. 2005; Rieck et al. 2014; Wang et al. 2011). Following Mahrt and Ek (1993), Pinty et al. (1989), and Teuling et al. (2017), we will use the term "forest breezes" to refer to vegetation-induced mesoscale circulations which form along the edges of forests.

Several observational studies have examined the occurrence of clouds over areas of sharp contrasts in vegetation and soil moisture and found that shallow convective clouds were favored to occur over hotter, drier surfaces adjacent to cooler, more humid areas (Chagnon et al. 2004; Esau and Lyons 2002; Mahrt and Ek 1993; Nair et al. 2011; Rabin et al. 1990; Sato et al. 2007; Taylor et al. 2012). By contrast, Brown and Arnold (1998) found that the initial development of shallow convective clouds during the day was more likely on the moist side of vegetation and soil type boundaries, but that deep convective clouds were equally likely to develop on either side of the boundaries. While not directly examining clouds, Phillips et al. (2022) analyzed data from the Great Plains Irrigation Experiment (GRAINEX) field campaign in Nebraska to determine that the presence of irrigated areas on elevated terrain weakened diurnally driven upslope winds, which the authors speculated may likewise affect the development of clouds and precipitation.

In addition to observations, a number of idealized modeling studies examining the relationship between land surface characteristics and convection have been performed at various scales and patterns of surface heterogeneity. Large-eddy simulations (LESs) with checkerboard and striped patterns of land surface properties found that solenoidal mesoscale circulations developed on the boundaries of the cool/wet and warm/dry patches. These circulations lead to inflow, rising motion, and convection over the warm patches and suppression of convection and precipitation over the cool patches (Avissar and Liu 1996; Chen and Avissar 1994; Cheng et al. 2021; Cheng and McColl 2023; Cheng et al. 2023; Cioni and Hohenegger 2018; Emori 1998; Fogarty and Bou-Zeid 2023; Garcia-Carreras et al. 2011; Harvey et al. 2022; Hong et al. 1995; Kang and Bryan 2011; Lee and Kimura 2001; Lee et al. 2019; Lynn et al. 1998; Rieck et al. 2014, 2015; Wang et al. 2011). The inflow from the cool/wet to warm/dry patches, and rising motion over the warm/dry patches, also acts both to transport water vapor from the surface of cool/wet patches to warm/dry patches and to lift that water vapor into upper levels of the boundary layer over warm/dry patches (Avissar and Liu 1996; Chen and Avissar 1994; Cioni and Hohenegger 2018; Emori 1998; Harvey et al. 2022; Hong et al. 1995; Kawase et al. 2008; Lee et al. 2019; Rieck et al. 2014). This increase in upper-PBL water vapor acts to lower the lifting condensation level (LCL) and the level of free convection (LFC) over the warm/dry patch, at the same time as the warm temperatures and rising motions raise the height of the PBL. Together, these factors combine to encourage the development of deep convection over the warm/dry patch. At the same time, divergence aloft over the warm/dry patch and convergence and sinking aloft over the cool/wet patch act to bring dry air from higher in the atmosphere down closer to the surface of the cool/wet patch, while simultaneously stabilizing the atmosphere through adiabatic warming of the subsiding air. This suppresses convective development over the cool/wet patch.

The size of the land surface patches greatly affects the locations and strengths of these land surface–induced circulations and hence the convection they initiate. Too small of a patch may not allow sufficient temperature contrasts to build to drive strong mesoscale circulations (Chen and Avissar 1994; Lynn et al. 1998). However, the solenoidal mesoscale circulations which develop along land surface boundaries also propagate in time toward the center of the warm patch (Chen and Avissar 1994; Hong et al. 1995; Lynn et al. 1998; Rieck et al. 2014, 2015). As a result, too large of a patch will mean that the circulations propagate too slowly to collide in the center of the patch before diurnal heating weakens, preventing them from helping initiate convection in the patch center (Lynn et al. 1998). Chen and Avissar (1994) hypothesized that there is an "ideal patch size" which allows strong circulations to develop and collide in the center of the patch while conditions are still favorable for further convective storm development. They determined that this ideal patch size is equivalent to the local Rossby radius of deformation, which was approximately 100 km in their simulations. Lynn et al. (1998) further demonstrated this concept in their 2D simulations, where patches 128 km wide allowed for a collision of circulations and intense precipitation, while patches 256 km wide did not produce a collision of circulations before conditions were no longer favorable for convection. Hong et al. (1995) demonstrated that this ideal patch size depends on atmospheric stability; larger static stability decreases the ideal patch size by favoring the development of narrower circulations, while smaller static stability increases the ideal patch size by favoring wider circulations.

In addition to these idealized studies, several case study simulations of regions with vegetation/soil moisture heterogeneity have also identified these mesoscale circulations. As with the idealized studies above, they have found that these circulations favor convection on the warm and dry sides of gradients in land surface properties (Branch and Wulfmeyer 2019; Chen et al. 2020; Cheng and Cotton 2004; Fast et al. 2019; Kawase et al. 2008; Mascart et al. 1991; Sato et al. 2007).

Despite ample evidence from modeling and observations demonstrating that heterogeneous land surface properties induce mesoscale circulations which affect convection, many outstanding questions remain. In particular, none of the idealized modeling studies described above have examined a coastal environment. The interaction of sea-breeze circulations with land surface–induced circulations has not been well explored, and the combined effects of these interacting mesoscale circulations on convection initiation are unclear. Furthermore, although Rieck et al. (2015) explored the role of cold pools in increasing the propagation speed of these circulations, they did not demonstrate whether or how this affected the collision of the circulations at the center of the dry patch. Finally, the modeling studies described above have compared variations in prescribed surface fluxes, soil moisture, vegetated versus bare soil surfaces, or single

TABLE 1. Settings used for all RAMS simulations.

Model parameter	Value
Grid	Arakawa C grid (Arakawa and Lamb 1977)
Horizontal grid spacing (m)	500
Horizontal domain	802 × 402 grid points
Vertical grid spacing (m)	Stretched (30–300)
Vertical levels	105
Time step (s)	1.5
Simulation duration (h)	18
Thermodynamic initialization	0528 UTC 17 Jun 2022 La Porte, Texas, sounding (Keeler et al. 2022)
Zonal boundary conditions	Periodic
Meridional boundary conditions	Radiative (Klemp and Wilhelmson 1978)
Upper boundary condition	Rigid model top at 23 km
Surface parameterization	LEAF-3 (Walko et al. 2000)
Soil levels	8 levels from −0.5 to −0.09 m
Soil type	Clay loam
Soil moisture	0.19 m^3 m^{-3}
Sea surface temperature	300 K (held constant throughout the duration of the simulation)
Microphysical scheme	Two-moment bulk microphysics with eight hydrometeor species (Saleeby and Cotton 2004)
Radiation scheme	Two-stream radiation, with tendencies updated every 10 min (Harrington 1997)
Aerosol initialization	450 cm^{-3} at surface, decreasing exponentially with height (Saleeby and van den Heever 2013)
Aerosol–radiation direct effects	On (Saleeby and van den Heever 2013)
Aerosol sources and sinks	Aerosol depletion from nucleation and wet/dry deposition (Saleeby and van den Heever 2013)
Turbulence scheme	Smagorinsky (1963) with modifications by Hill (1974) and Lilly (1962)
Coriolis force	Inactive
Latitude (°)	30
Day of year	17 Jun

parameters of the vegetation [such as LAI in Rieck et al. (2014, 2015)], but they have not contrasted multiple vegetation types with different surface roughnesses, albedos, leaf properties, or vegetation fractions.

The goal of this study is to examine two outstanding questions related to landscape heterogeneity-induced convection in coastal environments. 1) How does the interaction of the sea breeze with landscape heterogeneity-induced circulations affect the location and impacts of convection? 2) How do cold pools produced by the initial convection associated with these circulations affect the further development of these circulations and subsequent convection?

2. Experimental design

To examine the impact of heterogeneous land surfaces on convection in a coastal environment, we ran six idealized simulations using the Regional Atmospheric Modeling System (RAMS), a nonhydrostatic, cloud-resolving model (Cotton et al. 2003). Common model settings for all simulations are provided in Table 1.

The impetus for this study was the Experiment of Sea Breeze Convection, Aerosols, Precipitation, and Environment (ESCAPE), a field campaign conducted around Houston, Texas, in the summer of 2022 (Kollias et al. 2024) alongside the Tracking Aerosol Convection Interactions Experiment (TRACER) (Jensen et al. 2023). The Houston area is a coastal location which also possesses many different land surface types, including the urban core and sprawling suburbs of Houston itself, coniferous forest to the north and east of the city, and agricultural pasture and cropland to the south and west (Fig. 1). We wanted to examine how the presence of land surface heterogeneity could have affected the development of deep convection in an atmospheric environment similar to that observed during ESCAPE/TRACER. As such, we designed simulations which presented coastal domains with land surfaces representative of those found around Houston (described in more detail below). All simulations prescribed an ocean area south of a land area with a straight east–west coastline (Fig. 2). The ocean extended 150 km north from the southern boundary of the model domain and spanned the entire 200-km east–west width of the domain (the ocean is shown by the blue area in Fig. 2). The ocean surface temperature was held fixed at 300 K throughout the duration of the simulation, a temperature representative of that found in the Gulf of Mexico near Houston in June 2022 (Reynolds et al. 2002). North of the ocean was a land area extending 250 km in the north–south direction to the northern boundary of the domain and the entire 200-km east–west domain width. To prevent the complicating effects of topography, all land areas were completely flat with a terrain height at sea level.

A set of six simulations were run with varied land surface types (Fig. 2). These simulations were initialized with volumetric soil moisture of ~0.19 m^3 m^{-3} (which corresponds to a saturation fraction of 0.4 for the clay loam soil type used in the simulations), representative of soil conditions found in the Houston area on 17 June 2022 (Dashtian and Young 2023). During the ESCAPE campaign of 30 May–28 June 2022, southeastern Texas experienced a severe drought resulting in dry soils. All six simulations were also initialized with a horizontally

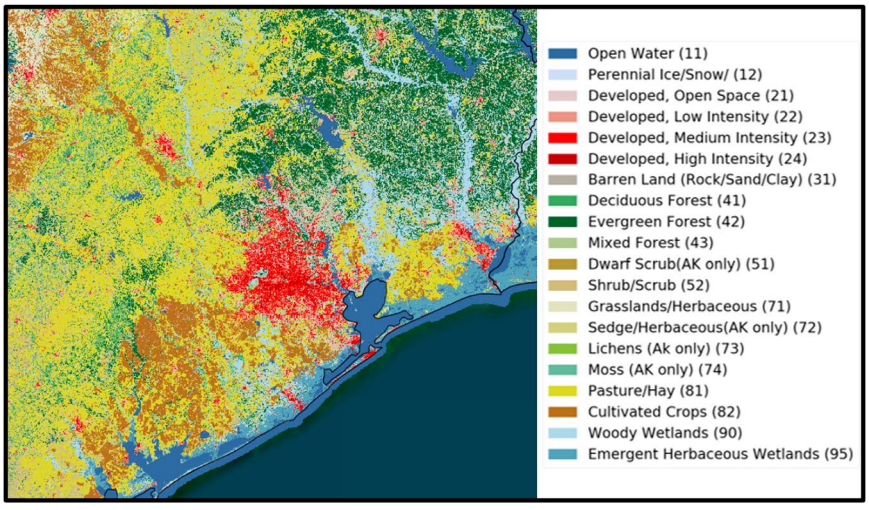

FIG. 1. National Land Cover Database map of the Houston area, courtesy of the United States Geological Survey (DeWitz and USGS 2021). The map depicts the area between approximately 28.5°–31.5°N and 97.4°–93.6°W (approximately 365 km north–south and 330 km east–west extent). Colors corresponding to each land-cover category are shown in the legend on the right. Thin black lines indicate state borders.

uniform southerly background wind profile which increased logarithmically with height from 2 m s^{-1} at the surface to 8 m s^{-1} at 900 hPa. This wind profile was representative of that observed in the PBL on 17 June 2022, while the constant wind profile above the boundary layer simplified analysis (Keeler et al. 2022). The observed wind profile on this day did vary weakly above the PBL, but there was little vertical wind shear present above the PBL which would have affected the convective organization.

The only differences between the six simulations were the type and spatial distribution of land cover north of the ocean. Simulations 1–3 used uniform land surface types: UP—uniform pasture, UF—uniform coniferous forest, and US—uniform suburbs. (Figs. 2a–c). We chose these land surface types to represent the landscape found in and around Houston, with different land surface types adjacent to one another and near the coast. Simulations 4–6 employed a striped land surface pattern (Figs. 2d–f). The leftmost and rightmost 50 km from the zonal boundaries consisted of one land type, while the center 100 km was another land type. Because of the periodic zonal boundary conditions, this is identical from a modeling perspective to having two 100-km-wide stripes adjacent to one another. Simulation PF consisted of a center stripe of coniferous forest surrounded by pasture (Fig. 2d), simulation SF consisted of a center stripe of coniferous forest surrounded by suburbs (Fig. 2e), and simulation SP consisted of a center stripe of pasture surrounded by suburbs (Fig. 2f). Table 2 illustrates key properties of the three different land surface types present in the simulations.

As stated above, the simulations used periodic boundary conditions in the east–west dimension and made use of radiative boundary conditions in the north–south dimension. The Coriolis force was disabled in all six simulations. This was done for simplicity purposes, as we wanted to focus on the basic interactions of vegetation-induced circulations perpendicular to an idealized sea breeze. As Anthes (1978), Antonelli and Rotunno (2007), Simpson (1996), and Yan and Anthes (1987) have found, the Coriolis force has only small effects on the strength, structure, and horizontal extent of the sea breeze during times of peak diurnal heating. Therefore, we would not expect the Coriolis force to significantly affect forest breezes which form under strong diurnal heating. However, the absence of the sea breeze allows for complete symmetry on both sides of the vegetation stripes and for the forest breezes to maintain their orientations parallel to the vegetation stripes, simplifying analysis.

The initial thermodynamic profile for our simulations was obtained from the 0538 UTC 17 June 2022 sounding launched from the Atmospheric Radiation Measurement (ARM) sounding site at La Porte, Texas, during the TRACER field campaign (Keeler et al. 2022). This sounding was chosen because 17 June 2022 was a day which featured widespread isolated convection over the Houston area (Kollias et al. 2024). To disrupt initial atmospheric homogeneity and encourage more realistic boundary layer behavior, small random perturbations were applied to the potential temperature field at simulation initialization. These perturbations were between −0.5 and 0.5 K at the lowest model level, decreasing exponentially with height in each column to 1 km, at which point the perturbations in each column were set to zero. This was done to confine turbulent motions early in the simulation to near the surface and within the nocturnal boundary layer. Following initialization, the temperature perturbations and associated turbulent motions were allowed to evolve freely and were not restricted to the lowest 1 km of the simulation.

3. Results

a. *Uniform land surface simulations*

A weak sea breeze develops in all simulations starting at approximately 1000 LT [identifiable as a boundary in 200-m

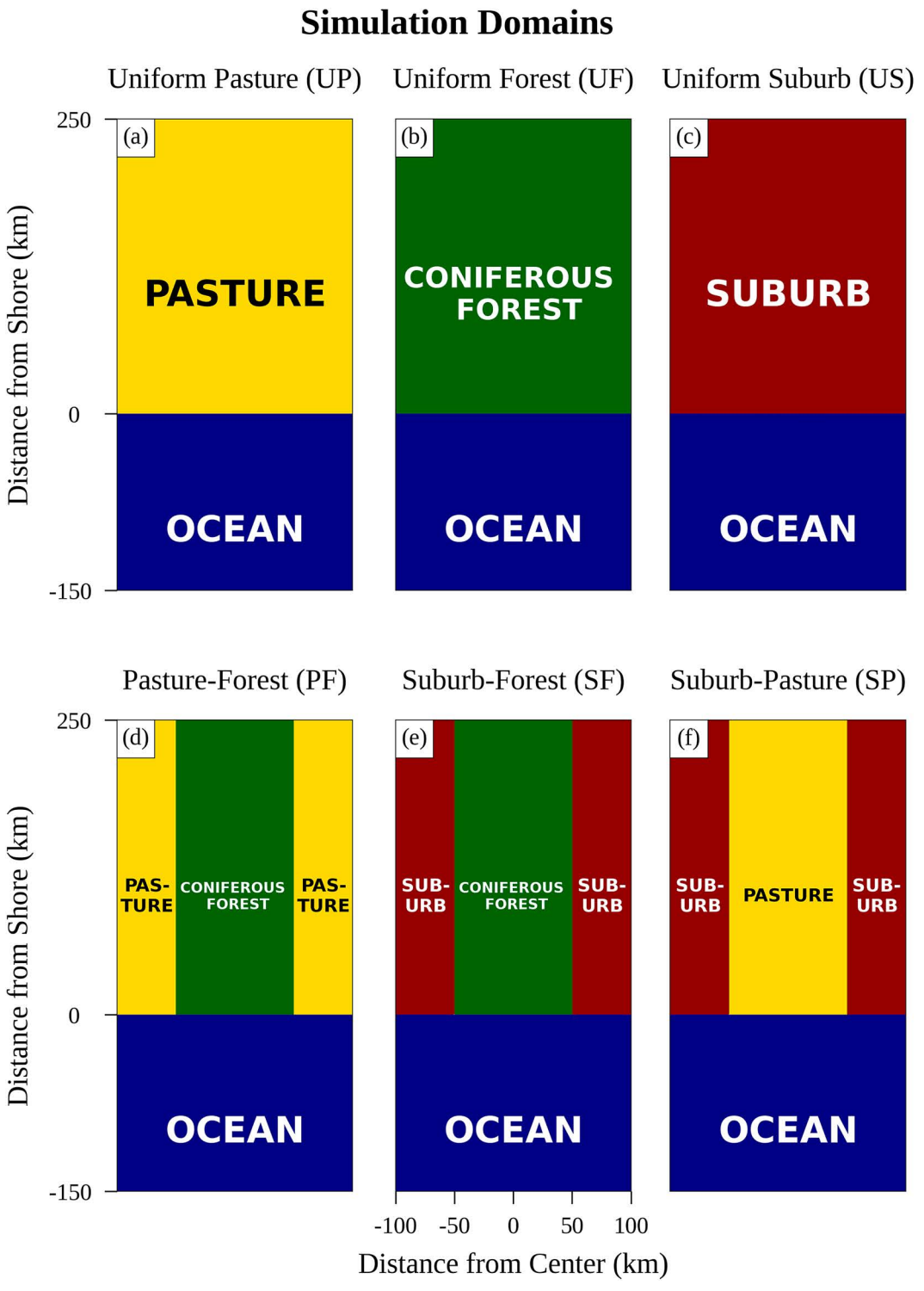

FIG. 2. (a)–(f) Comparison of land surface properties characterizing the six model domains used in the study. Land surface types in each area of the domain are labeled. Note that the meridional spatial dimensions marked in (a) and (d) and the zonal spatial dimensions marked in (e) apply to all six simulations.

TABLE 2. Key properties of vegetation types used in simulations.

Land surface type	Pasture	Suburbs	Coniferous forest
Vegetation broadband shortwave albedo	0.283	0.305	0.154
Vegetation fraction	0.430	0.395	0.774
Total surface broadband shortwave albedo	0.179	0.184	0.129
Leaf area index	0.909	0.525	5.890
Vegetation height (m)	1	6	20
Total roughness length (m)	0.100	0.602	2.716

water vapor mixing ratio at $y = \sim+50$ km (y being the distance north of the shoreline) in Fig. 3]. The sea-breeze front moves inland throughout the day, reaching $y = +75$ km at approximately 1500 LT, though this timing varies slightly over different land-cover types (not shown). In addition to the sea breeze, horizontal convective rolls (HCRs) developed in all three uniform land surface simulations. These HCRs are parallel to the mean northward background wind and have rising and sinking branches, consistent with prior observations of HCRs (Sykes et al. 1988; Weckwerth et al. 1996). The HCRs are visible in Fig. 3 as alternating north–south-oriented bands of larger and smaller vapor mixing ratio and in Fig. 4 as bands of greater and lesser temperature. Note that plan views of water vapor mixing ratio are plotted at an altitude of 200 m, while near-surface air temperatures are plotted at an altitude of 15 m. This is because these altitudes corresponded to the greatest horizontal variability in water vapor mixing ratio and temperature, respectively. Our discussions of energy balance over different land surface types will examine these temperature and moisture differences in the surface layer and discuss their effects on PBL structure.

Deep convection [defined here as storms with cloud-top heights above 6 km above ground level (AGL) following Lee et al. (2019)] develops along and inland of the sea-breeze front in all three uniform land surface simulations. However, even though deep convective storms occur throughout the domains of the UP, US, and UF simulations, they are strongest with respect to cloud-top heights (Figs. 5a–c) and vertically integrated condensate (supplemental animations 1a–c and 2a–c in the online supplemental material) along and just inland of the sea-breeze front. In the UF simulation, for example, storms with cloud-top heights above 10 km AGL and vertically integrated condensate greater than 20 mm liquid equivalent are found primarily in a zonal line which moves with the sea-breeze front until 1440 LT, after which strong convective storms begin to develop inland of this line (supplemental animations 1b and 2b).

In simulation UF, the first deep convection emerges at 1250 LT, while in simulations US and UP the onset of deep convection is delayed until 1400 and 1410 LT, respectively. The presence of deep convection in the UF simulation, and its absence in the UP and US simulations, at 1330 LT is evident in Figs. 5a–c. The difference in convective behavior between the UF and UP/US simulations is primarily driven by the greater near-surface air temperature over the forest relative to the pasture or suburbs. The pasture and suburbs have nearly identical domain-mean 15-m air temperatures of approximately ~305.5 K at 1200 LT (Figs. 4a,c) and ~308.7 K at 1500 LT (supplemental animations 3a,c). By contrast, the coniferous forest has a domain-mean 15-m air temperature of approximately ~308.3 K at 1200 LT (Fig. 4b) and ~309.9 K at 1500 LT (although by 1500 LT, cold pools from convective storms are widespread over the forest, contaminating temperature estimates) (supplemental animation 3b).

The reasons for the greater near-surface air temperatures over the forested areas are twofold: First, the greater vegetation fraction of the coniferous forest as opposed to the pasture or suburbs (Table 2) means that more of the incoming solar radiation is absorbed by the vegetation rather than the soil. This in turn allows more energy to be transferred to the canopy layer as opposed to being stored in the ground (Mascart et al. 1991). Second, the greater vegetation roughness length of the coniferous forest as opposed to the pasture or suburbs allows for more efficient mixing of this canopy layer air with the overlying atmospheric air, thereby facilitating more sensible heating of the atmosphere (Figs. 6a–c) (Cheng and McColl 2023; Mahrt and Ek 1993; Mascart et al. 1991; Pinty et al. 1989; Teuling et al. 2017). These greater near-surface air temperatures over the forest increase the PBL height in the UF simulation compared to the UP and US simulations (discussed further below in section 3b). This means that air parcels can more easily reach their LCL and LFC in the UF simulation, allowing an earlier onset of deep convection compared to the UP and US simulations.

The drought conditions present in Houston on 17 June 2022, and reflected in the initially dry soils in the simulation, lead to a counterintuitive finding: The reduced latent heating over the forest relative to the pasture or suburbs is due to the greater vegetation fraction over the forest. Because the soils are dry throughout their entire depth in all simulations, stomatal resistances of the forest, pasture, and suburbs are large, preventing almost all transpiration. As a result, what little latent heat flux does occur is driven almost entirely by direct evaporation from the soil. Because little radiation reaches the soil under the forest due to the forest's large vegetation fraction (Table 2), limited energy goes into evaporating water from the soil under the forest, thereby reducing latent heat flux over the forest. By contrast, more radiation is able to reach the soil through the smaller vegetation fractions of pasture and suburbs to evaporate water from there. The differences between forest and pasture and suburbs are visible in Figs. 7a–c, where the surface latent heat fluxes over the forest in the UF simulation are smaller than those over the pasture and suburbs in the UP and US simulations. Partially as a

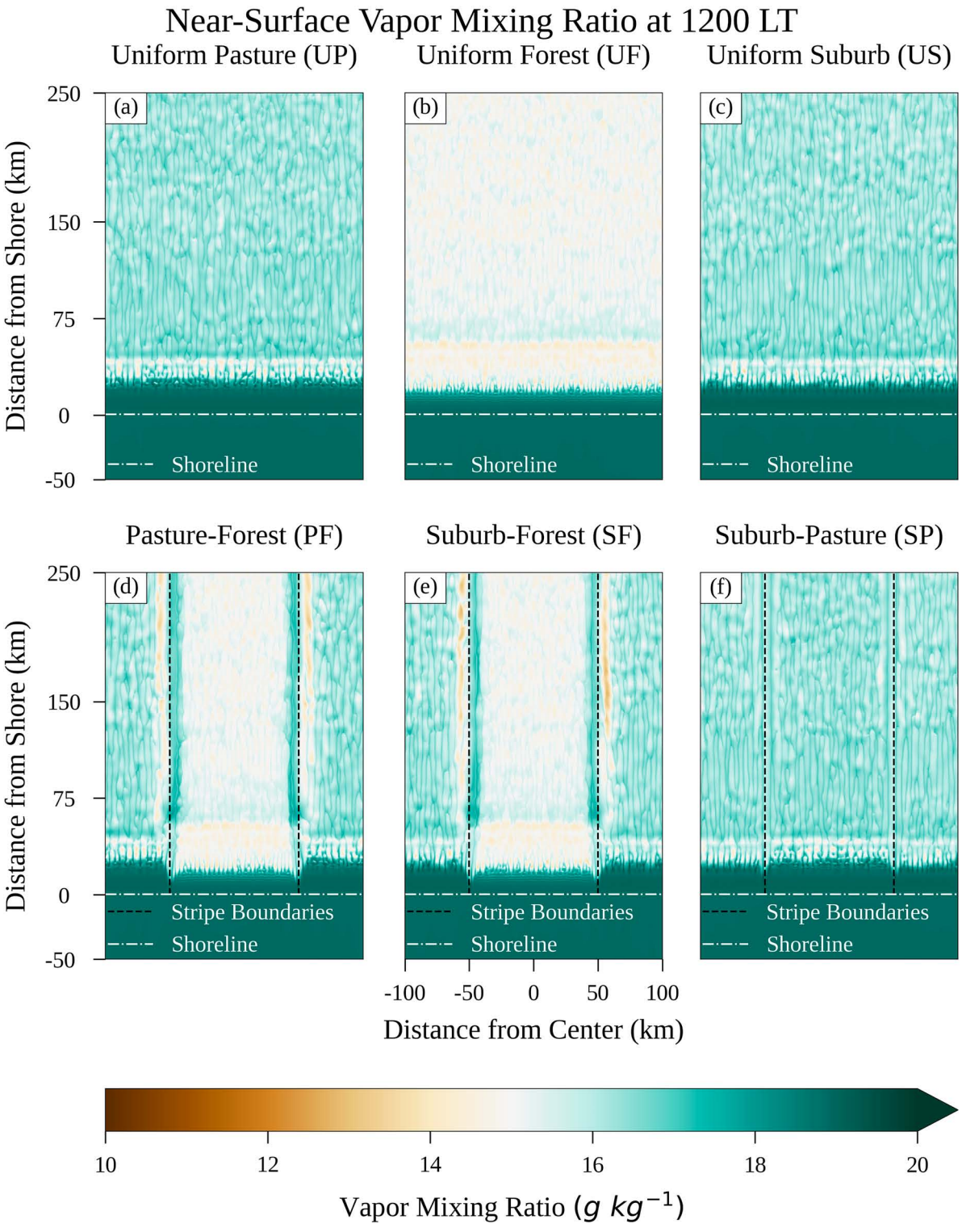

FIG. 3. Plan view of water vapor mixing ratio at 200 m AGL at 1200 LT. Low-level water vapor is reduced over the forest compared to the pasture and suburbs. The white dashed line indicates the shoreline, while the black dashed line indicates boundaries between land surfaces. The southernmost 100 km of the ocean has been omitted from this and similar plots.

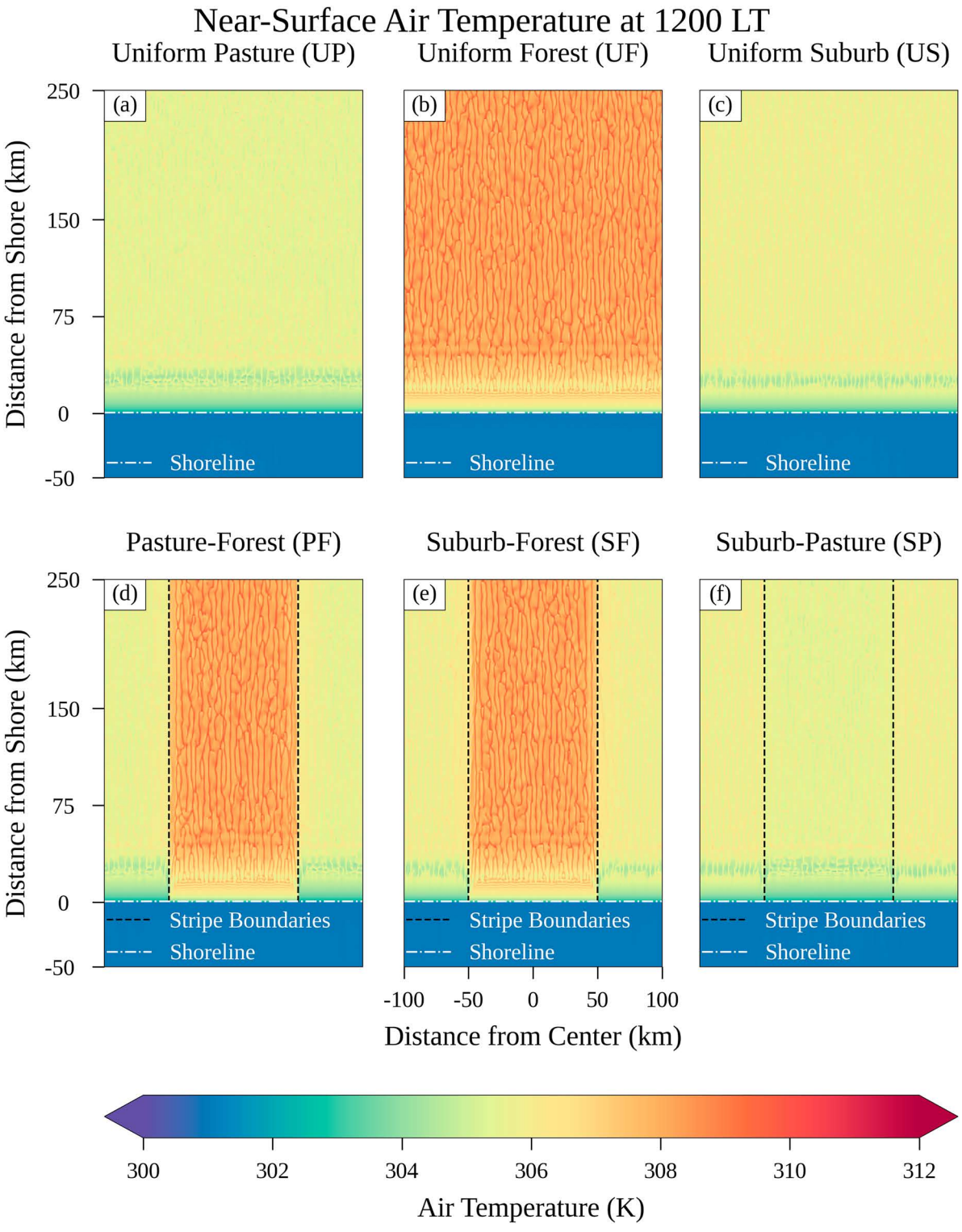

FIG. 4. As in Fig. 3, but for near-surface (15 m AGL) air temperature at 1200 LT. Near-surface air temperatures are greater over the forest than over the pasture or suburbs.

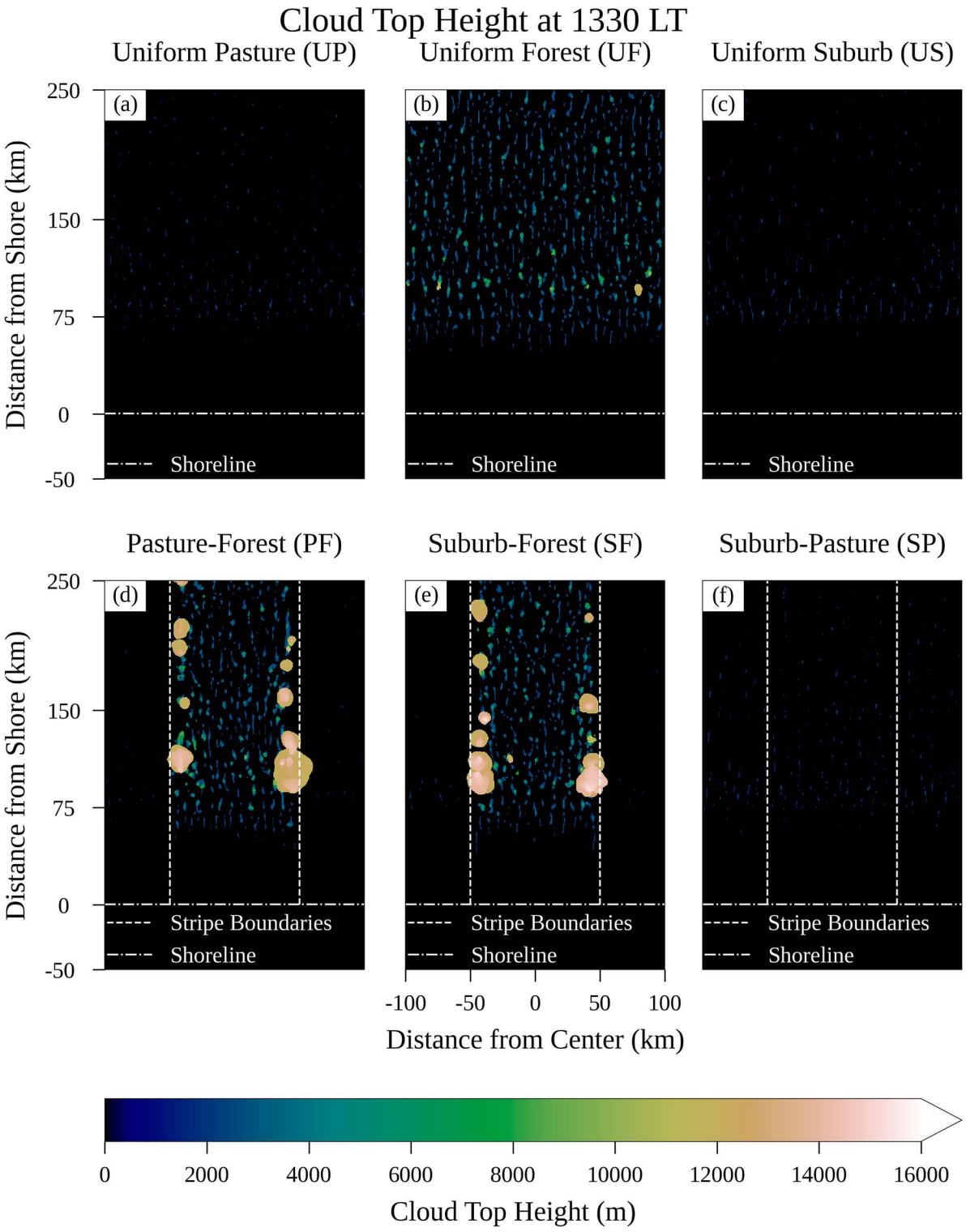

FIG. 5. Plan view of cloud-top heights at 1330 LT. Coverage of high cloud tops is greater in simulations PF and SF than in the other four simulations. The shoreline and land surface boundaries are denoted by horizontal and vertical white dashed lines, respectively.

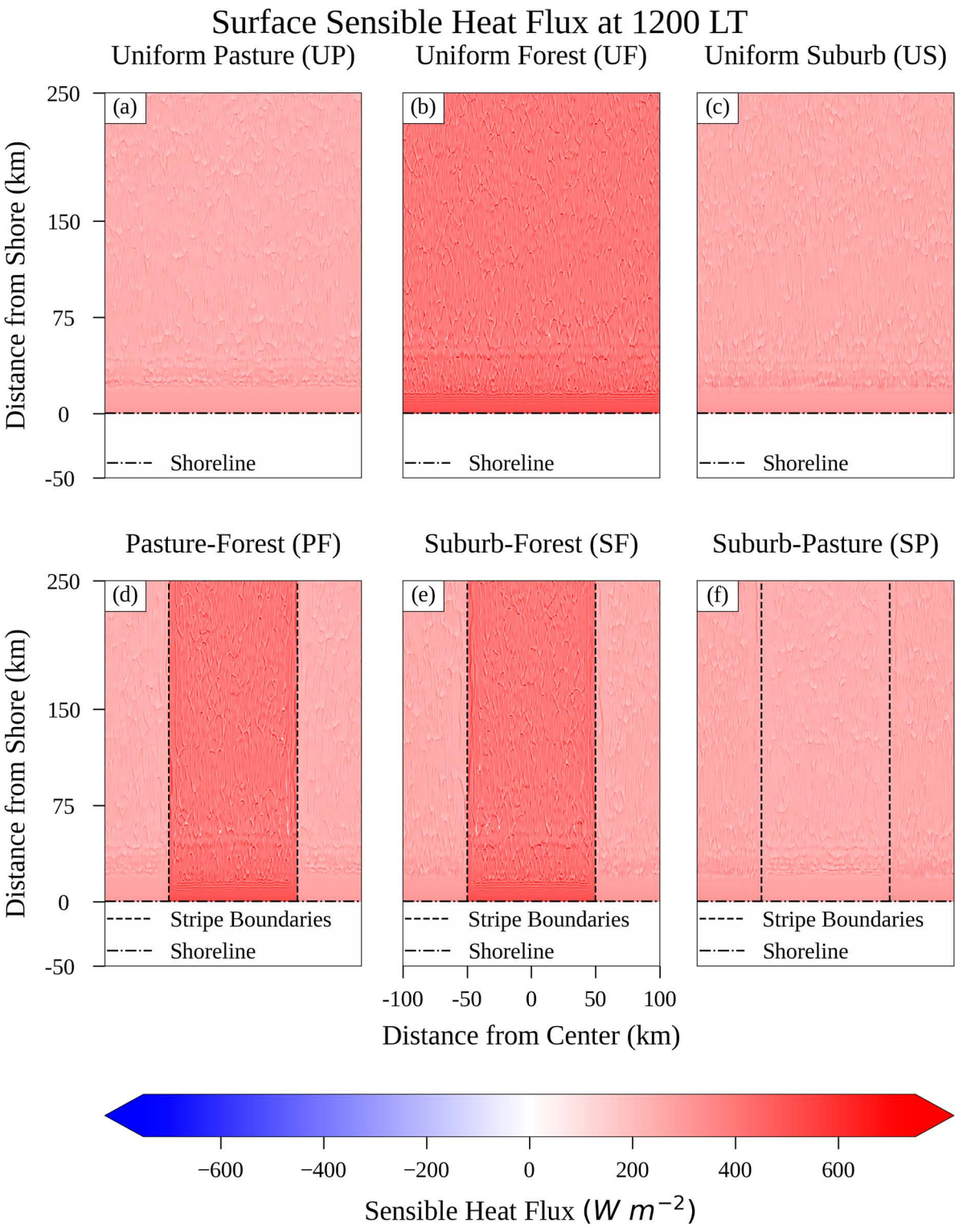

FIG. 6. As in Fig. 3, but for surface sensible heat flux at 1200 LT. Sensible heat flux is greater over the forest relative to the pasture and suburbs.

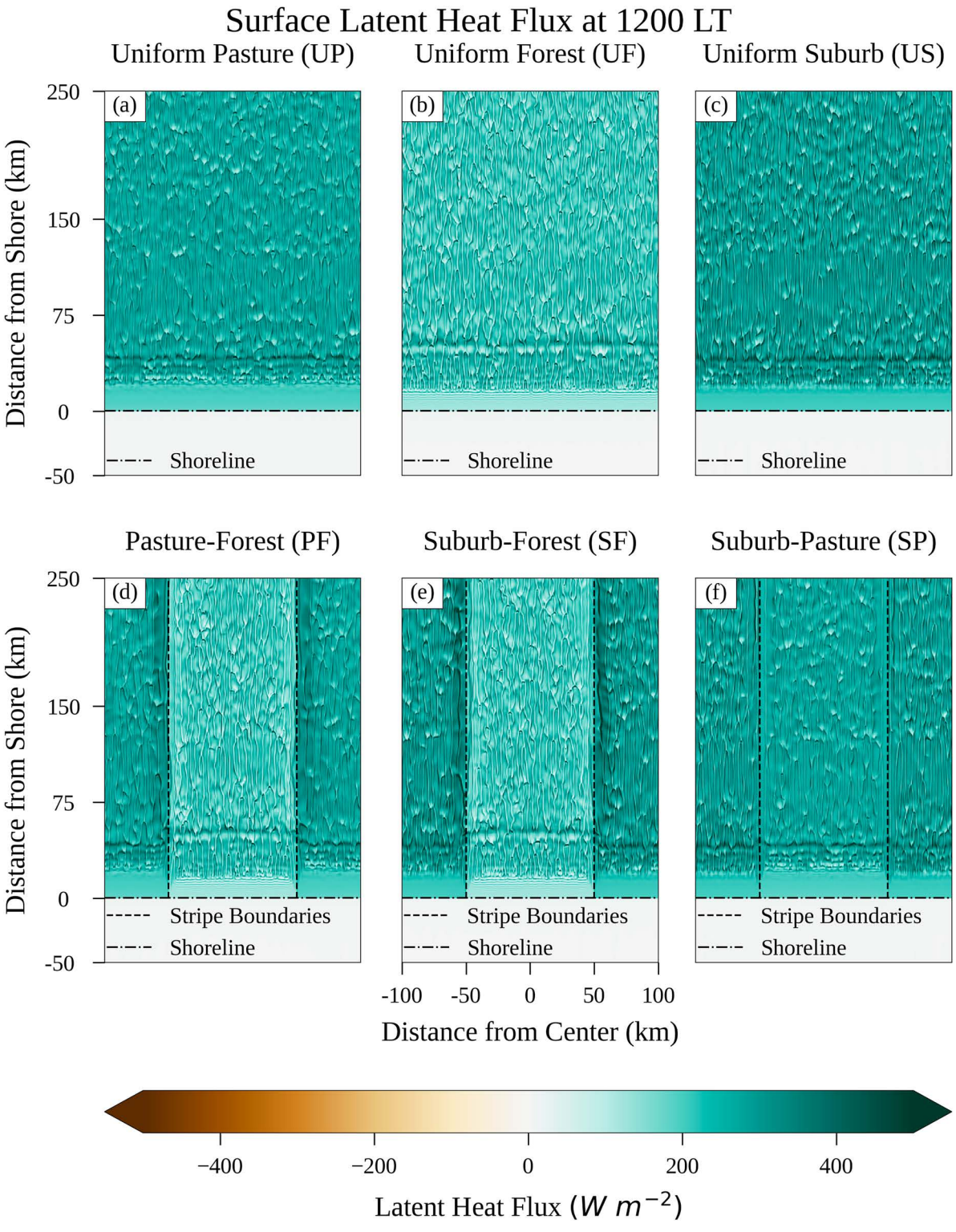

FIG. 7. As in Fig. 3, but for surface latent heat flux at 1200 LT. Latent heat fluxes are larger over the pasture and suburbs relative to the forest.

result of this greater latent heat flux over the pasture and suburb, vapor mixing ratios at 200 m above ground at 1200 LT are approximately ~15.0 g kg^{-1} over the forest and ~16.9 g kg^{-1} over the pasture and suburbs (Figs. 3a–c).

The differences in surface latent heat fluxes between the forest and pasture and suburbs are not the entire reason for the greater near-surface mixing ratios over the pasture and suburbs. The deeper boundary layer over the forest allows for greater vertical mixing of moisture compared to the pasture or suburbs, in which water vapor is more concentrated near the surface in the shallower and more stable boundary layers over these land surfaces. This reduction in near-surface water vapor mixing ratio increases the mean cloud-base height in the UF simulation, which at 1300 LT is 2010 m AGL, compared to 1531 m in the UP simulation and 1532 m in the US simulation (not shown).

The earlier emergence and greater coverage of strong deep convective storms in the UF simulation compared to the US/UP simulations lead to greater rainfall totals over the UF domain compared to the UP or US domains. The domain-mean accumulated rainfall in the UF simulation is ~0.910 mm, which is ~56% and ~42% more than the mean rainfall in the UP (~0.584 mm) and US (~0.641 mm) simulations, respectively (Figs. 8a–c).

South of approximately $y = +100$ km in simulations UP and US, and $y = +75$ km in the UF simulation, the boundary layer is cooled and moistened by the southerly inflow of marine air from the south. This results in a stabilized boundary layer with little CAPE (not shown) which inhibits deep convection close to the coast (Figs. 8a–c). To avoid including this marine-influenced air in our subsequent discussions of atmospheric properties and convection over different surfaces, subsequent comparisons of environmental variables and precipitation between simulations will focus only on the region north of $y = +100$ km.

b. *Striped land surface simulations*

The spatial distributions of accumulated rainfall in simulations PF and SF, which consist of a stripe of forest surrounded by stripes of pasture and suburbs, respectively, are different from those of the uniform land surface simulations. Again, the influence of the marine air in suppressing convection near the coast is clearly visible in Figs. 8d–f. While the coverage of rainfall was scattered more or less randomly inland of approximately 75 km from the coast in the UP, UF, and US simulations, the rainfall in simulations SF and PF is heavily concentrated over the forest, with comparatively little rainfall over the pasture or suburbs (Figs. 8d,e). The reasons for this are driven by thermodynamic differences between the forest and the surrounding pasture and suburbs and are discussed in more detail below.

In addition to there being more rainfall overall in the forested areas, a line of heavy rainfall is present in the center of the forest stripe in both the PF and SF simulations (Figs. 8d,e). Notably, the accumulated rainfall totals over the forest in these striped simulations are greater than those in the uniform land surface simulations. In simulations PF and SF, the mean rainfall over the forest is ~1.795 and ~1.859 mm, a ~97% and ~104% increase in accumulated rainfall per unit area compared to the uniform forest simulation.

While rainfall is enhanced over the forest, it is suppressed over the pasture and suburbs. Over the pasture in simulation PF, the mean rainfall is ~0.372 mm, a ~36% decrease from the average rainfall per unit area over the uniform pasture. Over the suburbs in simulation SF, mean rainfall is ~0.532 mm, a ~17% decrease from the average rainfall per unit area over the uniform suburbs.

Interestingly, even with the decreases in rainfall over the pasture and suburbs compared to the UP and US simulations, simulations PF and SF both have greater domain-total rainfall than any of the uniform land surface simulations. Simulation PF has a mean accumulated rainfall of ~1.084 mm over all land, which is ~19%, ~69%, and ~85% more than the mean accumulated rainfall in the UF, US, and UP simulations, respectively. Simulation SF has a mean accumulated rainfall of ~1.20 mm over all land, a ~31%, ~87%, and ~105% increase over the mean accumulated rainfall in the UF, UP, and US simulations.

In our discussions of the processes in the PF, SF, and SP simulations, we will refer to the situation at 1200 LT when discussing the convective environment over the forest, pasture, and suburbs. We choose this time because the environmental conditions and dynamical processes at that time are representative of those in the prestorm environment of the simulation.

As mentioned above, patterns of accumulated rainfall in the PF and SF simulations are driven by differences in thermodynamics between the forest and pasture/suburbs. Similar to the uniform land surface simulations, the forested areas in simulations PF and SF are approximately 3 K hotter than the surrounding pasture and suburbs, respectively, at 1200 LT (Figs. 4d,e). The greater near-surface air temperature over the forest is driven by larger sensible heating over the forest compared to the pasture/suburbs (Figs. 6d,e). At 1200 LT, the average sensible heat flux over the forest in simulations PF and SF is approximately 397.7 and 397.5 W m^{-2}, respectively. Over the pasture in simulation PF and the suburbs in simulation SF, sensible heat fluxes are just 240.0 and 251.8 W m^{-2}, respectively. At the same time, the average latent heat fluxes over the forest in simulations PF and SF are 216.4 and 216.2 W m^{-2}, compared to 284.68 W m^{-2} over the pasture in simulation PF and 300.61 W m^{-2} over the suburbs in simulation SF (Figs. 7d,e).

The different average vertical profiles of temperature and dewpoint over the forest and pasture can be seen in Fig. 9. The average vertical profile over the suburbs is not shown as it is nearly identical to that of the pasture. The vertical structure of temperatures over the forest and pasture in Fig. 9 indicates that the boundary layer over the forest is warmer and deeper than that over the pasture. As discussed above, this deeper boundary layer over the forest increases the vertical mixing of water vapor throughout the PBL over the forest compared to the pasture and suburbs. This vertical mixing increases atmospheric moisture in the upper boundary layer over the forest, reducing the effects of dry air entrainment on

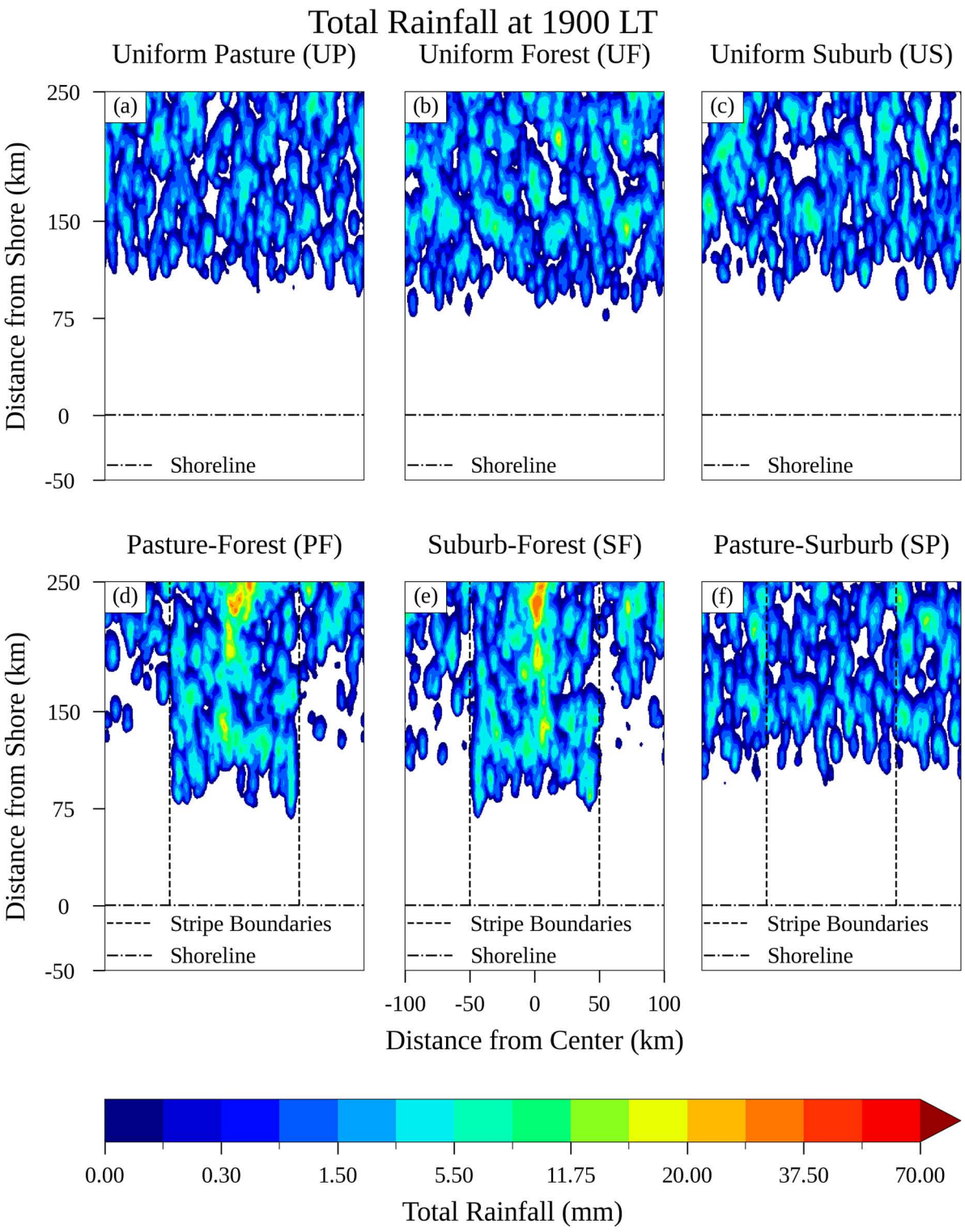

FIG. 8. As in Fig. 3, but for total accumulated rainfall over the course of the simulation. Rainfall in (d) and (e) is enhanced over the forest compared to over the surrounding pasture and suburbs, respectively. Note the nonlinear scale on the color bar.

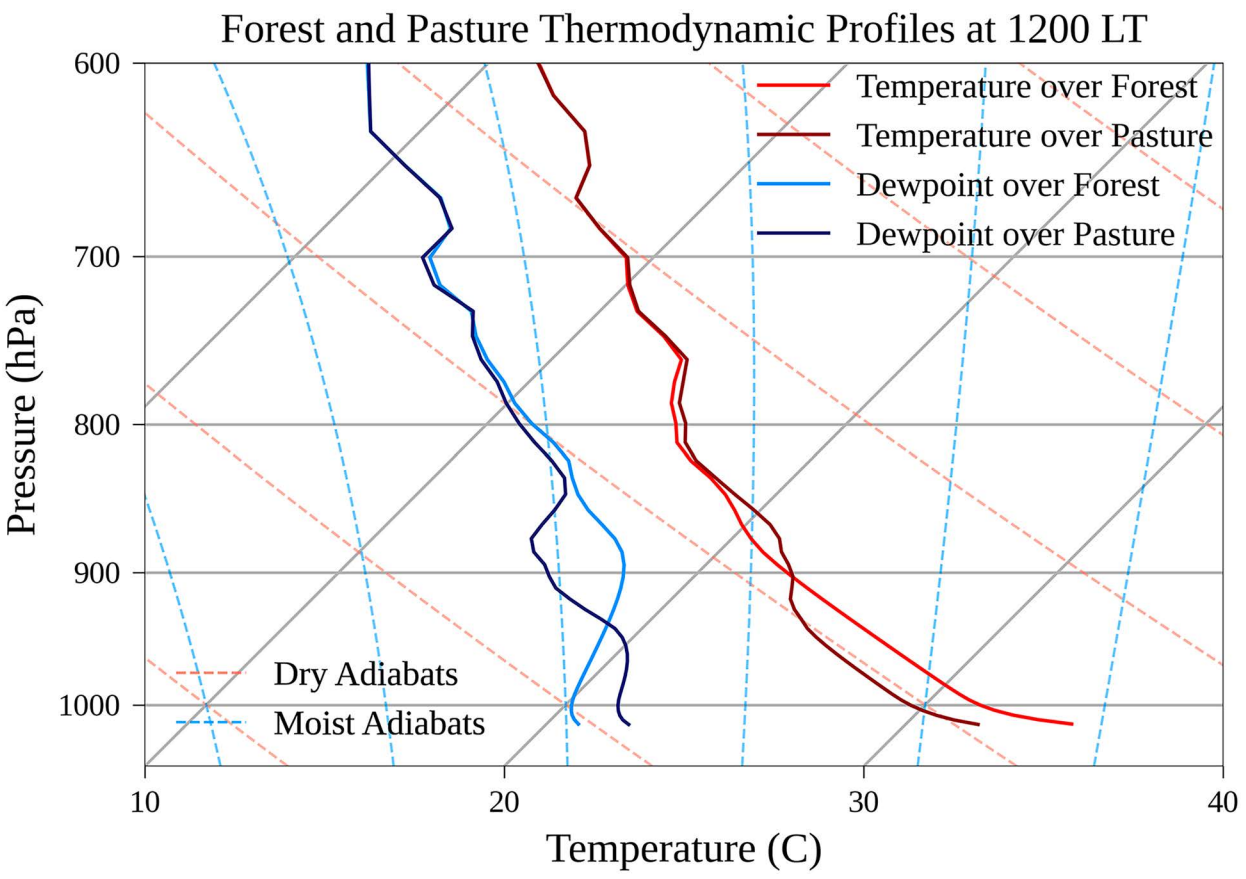

FIG. 9. Skew T–log$p$ diagram illustrating the warmer and deeper boundary layers of the coniferous forest compared to the pasture in the PF simulation. Temperature and dewpoint averaged over the center 50 km of forest north of $y = +100$ km are shown in red and light blue lines, respectively. Temperature and dewpoint averaged over the center 50 km of the pasture stripe north of $y = +100$ km are shown in maroon and dark blue lines, respectively.

parcels rising to their LCL and LFC compared to parcels over the pasture and suburbs.

The greater near-surface air temperature over the forest relative to the pasture or suburbs leads to smaller surface air pressures (Figs. 10d,e). The average surface pressure over the forest in both the SF and PF simulations at 1200 LT is approximately 1015.3 hPa, compared to 1015.7 hPa for both the suburbs and pasture in the SF and PF simulations, respectively. The reduced surface pressure over the forest in turn induces a forest breeze: a solenoidal mesoscale circulation similar to those described by Anthes (1984) and Pinty et al. (1989), with near-surface convergence over the forest (Fig. 11). The near-surface convergence associated with this forest breeze subsequently produces rising motion over the forest, divergence aloft above the forest, upper-PBL convergence and associated sinking motion over the pasture/suburbs, and near-surface divergence over the pasture/suburbs. A vertical cross section highlighting the forest breeze in the PF simulation is shown in Fig. 12.

The near-surface convergent branches of these forest breezes advect moister air from the pasture and suburbs stripes over the forest, similar to what has been seen in other idealized simulations in which low-level flow from cooler/wetter to hotter/drier patches advects moisture over the hotter/drier patch (Avissar and Liu 1996; Chen and Avissar 1994; Cioni and Hohenegger 2018; Emori 1998; Harvey et al. 2022; Hong et al. 1995; Kawase et al. 2008; Lee et al. 2019; Rieck et al. 2014). This moisture then rises just inside the forest edge, creating a plume of enhanced vapor mixing ratios which lowers the LFC and LCL, and increases moist static energy, locally (Fig. 12b).

The fact that deep convection initiates nearly simultaneously at 1230 LT in the PF and SF simulations just inside the forest edges suggests that the combination of direct mechanical lifting and low-level advection of moist air from the pasture/suburbs to the forest is sufficient to initiate deep convection just inside the forest edge. This convection initiation also occurs 20 min earlier than the initiation of deep convection in the UF simulation. These results indicate that the rising branches of the forest breeze accelerate the development of deep convection. Figures 5d and 5e clearly show the wide areal coverage of convective clouds with heights above 12 km (including convective anvils) just inside the edges of the forest stripe at 1330 LT, while only two storms have reached this height in the UF simulation.

In addition to the rising branches of the forest breeze along the edges of the forest, the sea breeze is an important, if not

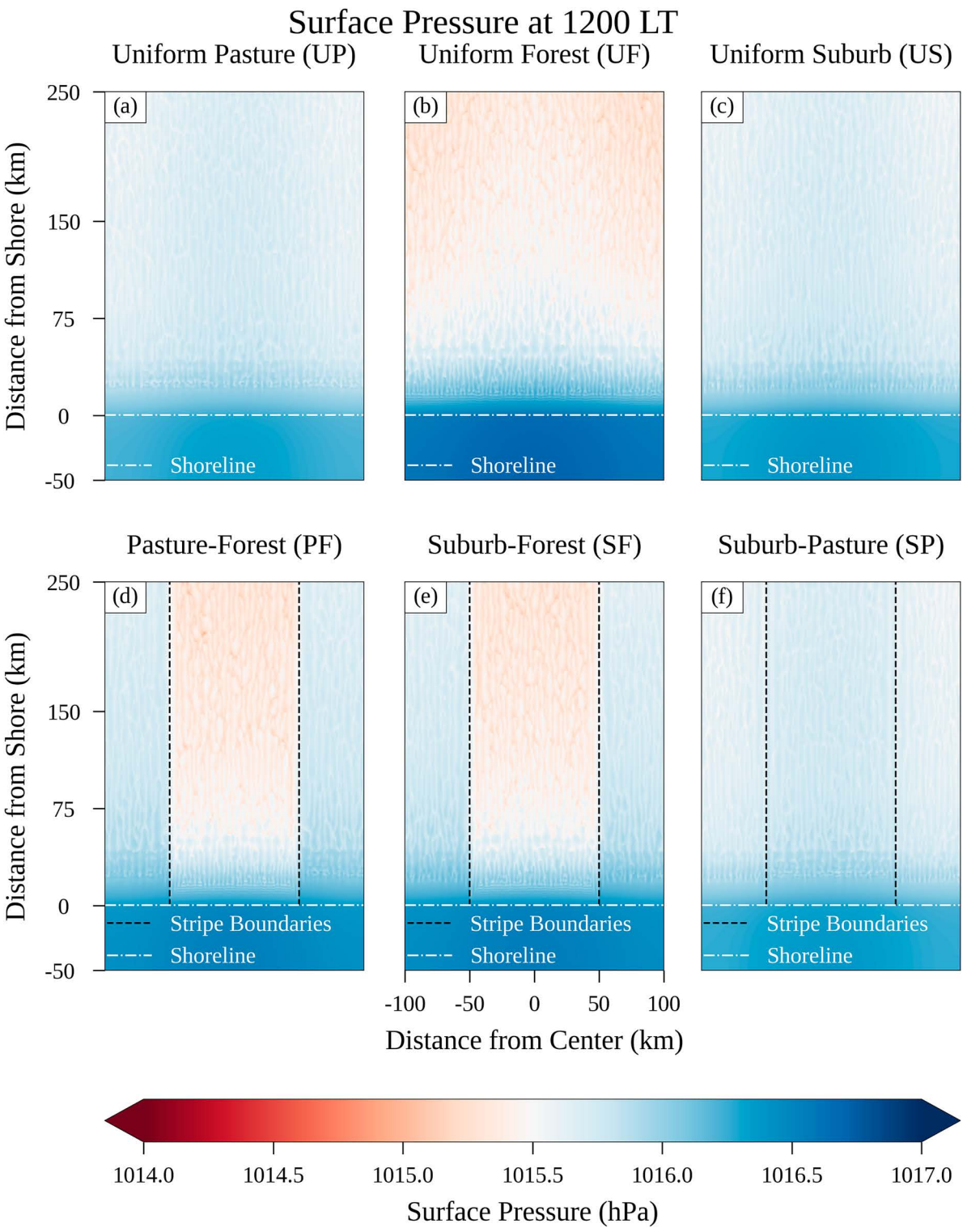

FIG. 10. As in Fig. 3, but for air pressure at the surface at 1200 LT. Surface air pressure is reduced over the forest compared to the surrounding pasture and suburbs.

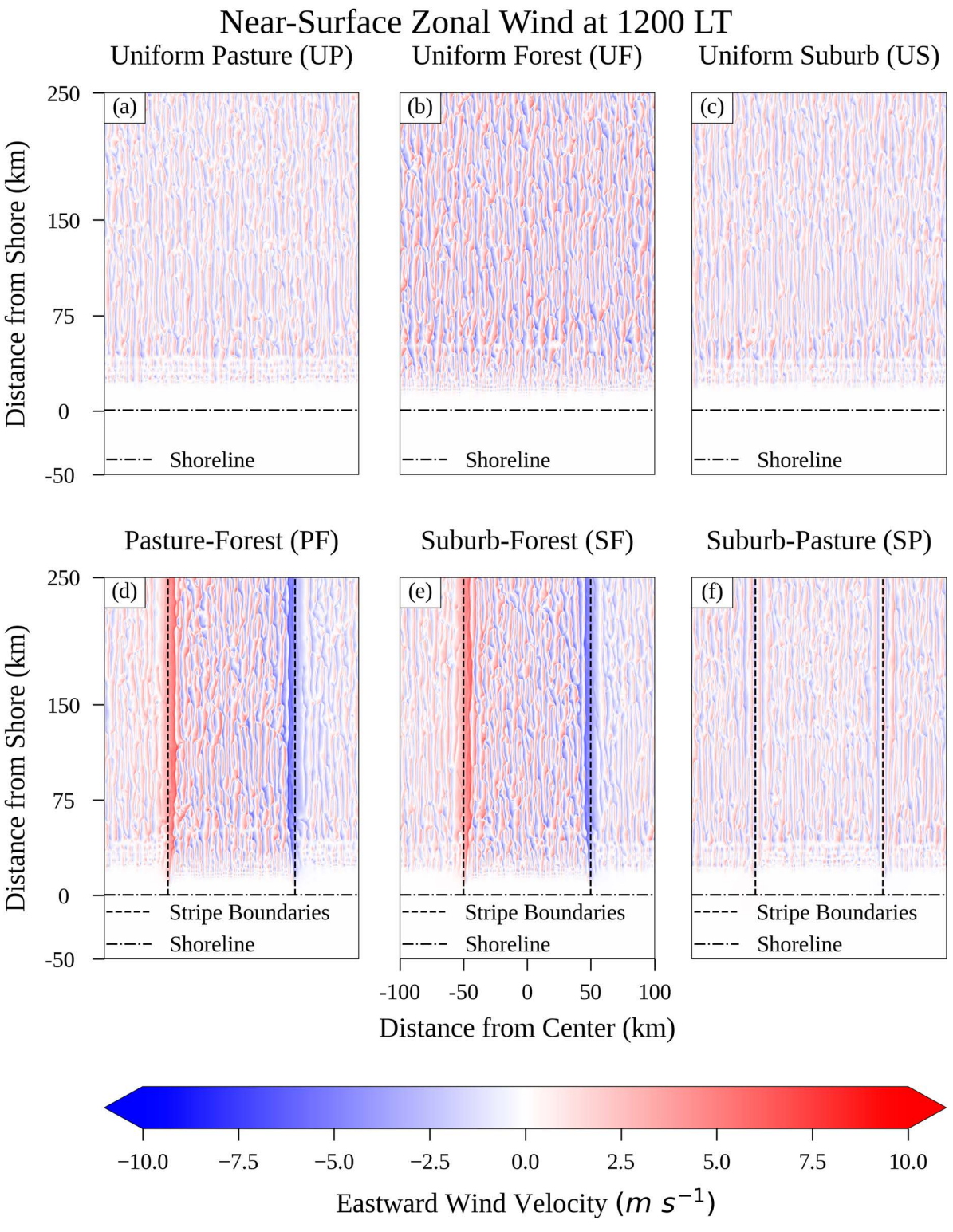

FIG. 11. As in Fig. 3, but for zonal winds at 200 m AGL at 1200 LT. Converging low-level zonal winds at the edge of the forest associated with the forest breeze are seen in (d) and (e).

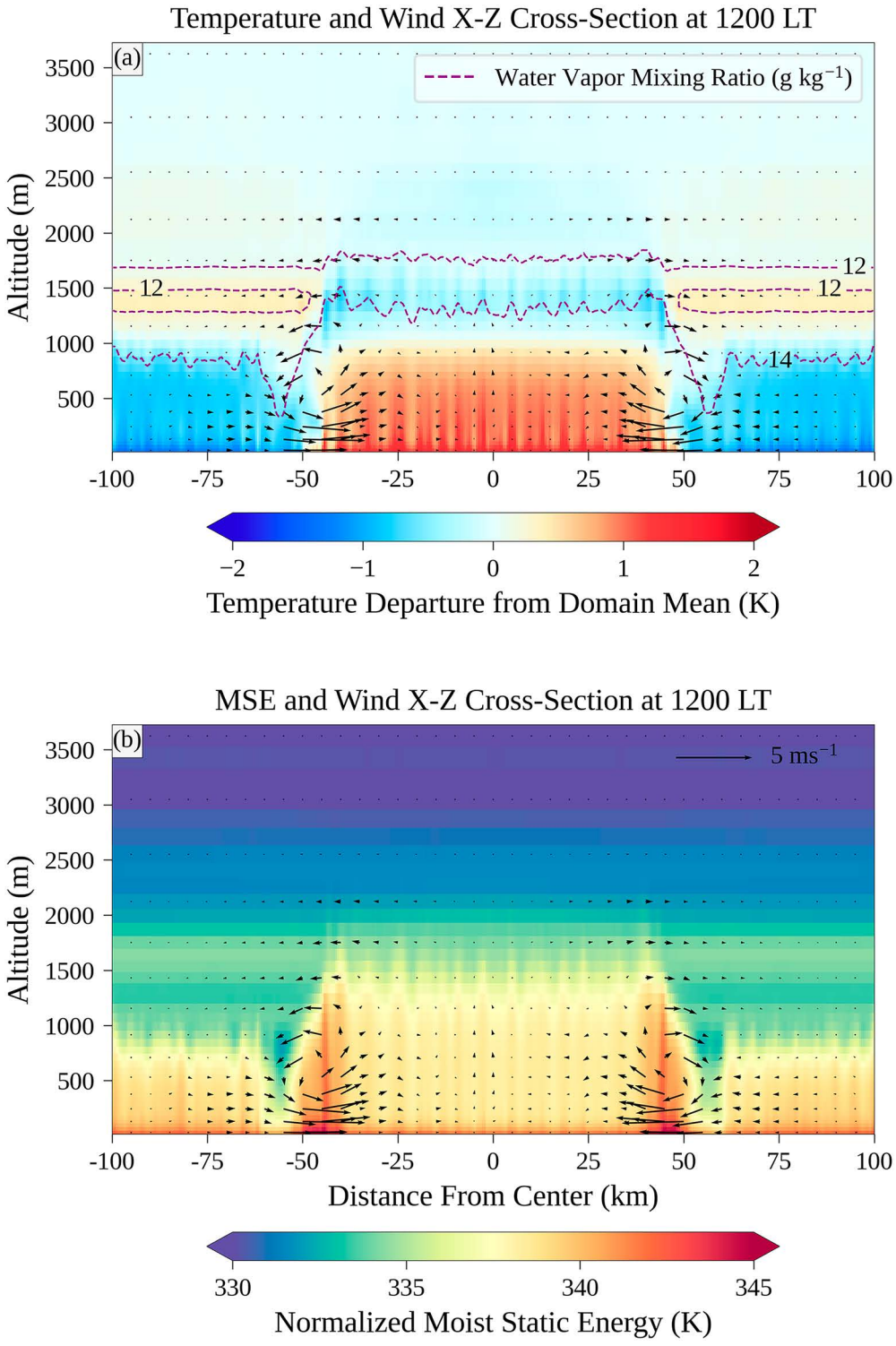

FIG. 12. (a) The X–Z vertical cross section showing wind (arrows) and air temperature (shaded), and (b) moist static energy divided by the specific heat capacity of dry air (shaded) at 1200 LT in the PF simulation averaged over the y direction from $y = +100$ km to $y = +250$ km. Contours of water vapor mixing ratio at 12 and 14 g kg^{-1} are plotted in (a) in magenta dashed lines.

primary, determinant in the initiation of the first storms in the PF and SF simulations. The first deep convective storms in both simulations occur along the edges of the forest at the meridional position of the sea-breeze front, which is approximately 75 km north of the coastline at this time (supplemental animations 1d,e). However, unlike the UF simulation in which the strong convective storms are restricted to the sea-breeze front until nearly 2 h after the emergence of the first deep convective storms, strong storms are visible along the forest edges well inland of the sea-breeze front by 1330 LT, only 70 min after the first emergence of deep convection in the PF and SF simulations (Figs. 5d,e). This indicates that the forest breeze induced by the vegetation boundary is more important than the sea-breeze front in determining the location and timing of convection initiation under certain environmental conditions. However, the behavior of the sea breeze depends on many environmental characteristics, including the difference between the sea surface and land surface temperature, background wind speed and direction, land soil moisture, land surface roughness length, Coriolis force, and boundary layer depth (Allouche et al. 2023; Grant and van den Heever 2014; Igel et al. 2018; Park et al. 2020; Yan and Anthes 1987). Though we did not conduct simulations varying these parameters, it is possible that doing so would reveal environmental regimes in which the sea breeze is a more important driver of convection initiation than the forest breeze.

While the forest breeze enhances convection over the forest, it suppresses it over the pasture and suburbs. Referring again to Fig. 12, we see clear sinking motions on the pasture side of the land surface boundary, which bring drier air from aloft down to the surface. In addition to this vertical transport of dry air, which can also be seen in Fig. 12a, the sinking branches of the forest breeze act to warm the atmosphere in this region by adiabatic compression. However, these two effects are localized to a small region along the edges of the pasture and suburbs and cannot account for the suppression of precipitation we see across the entire pasture and suburban regions in Figs. 8d and 8e.

At 1000 and 1500 m AGL, temperatures over the entire pasture and suburban stripes in the PF and SF simulations, respectively, are greater than the temperatures at those altitudes over the pasture and suburbs in the UP and US simulations (Fig. 12a). We suspect that this upper-PBL warming is the result of weak adiabatic compression which accompanies the diverging branches of the forest breeze. This warming stabilizes the upper levels of the boundary layer above the pasture and suburban stripes. This warming also increases the dewpoint depression at these levels, thereby exacerbating the effects of dry air entrainment on parcels rising to their LCL and LFC over the pasture and suburbs. Figure 9 indicates that the upper boundary layer over the pasture is warmer and drier than over the forest. The warming and drying effects of the diverging, downward branches of the forest breeze in the PF and SF simulations act to suppress convective development and precipitation over the pasture and suburban stripes relative to their uniform simulation counterparts.

Returning again to the forest stripe in the PF and SF simulations, the evolution of convection after the initiation of the first storms is quite different from the initial convective development. As the first storms along the forest edges mature, they produce precipitation. Cold pools develop as this precipitation evaporates and spread inward toward the center of the forest (supplemental animations 3d,e). These cold pools notably remain almost entirely confined to the forest stripe for many hours after the emergence of deep convection, likely as a result of the convergent flow into the forest from the forest breeze. They do expand inward toward the center of the forest stripe, reinforcing the pattern of inflow as they do so. As they expand inward, lifting along the cold pool edges triggers new convection further inside the forest. As these new cold pool-induced storms develop, they too produce cold pools which further reinforce the low-level inflow associated with the forest breeze. This process acts to propagate the low-level winds associated with the original forest breezes inward toward the forest center, as is seen in Fig. 13a between 1300 and 1500 LT. These results are in general agreement with those of Rieck et al. (2015). The two sides of this low-level inflow collide at roughly 1500 LT at $y = +125$ km at the center of the forest, although the collision happens approximately 30 min later at the northern end of the forest. Examining Fig. 13a, we should note that although the inflow does propagate inward without the assistance of cold pools between 1000 and 1300 LT, it does so slowly. Without assistance from cold pools in propagating the forest breeze inward toward the forest center, it is possible the inflow branches of the forest breeze may not have collided in the center of the forest at all.

The collision of low-level inflow branches of the forest breeze, and the convergence associated with this collision, triggers intense mechanical lifting in the center of the forest, initiating intense convection along the centerline of the forest from approximately $y = +125$ km to $y = +250$ km. These convective storms quickly grow in intensity, with heights of over 14 km and vertically integrated condensate levels exceeding 50 mm liquid equivalent in many storms (supplemental animations 1d,e and 2d,e). Given the intensity of these storms, it is unsurprising that they lead to heavy precipitation totals, which are reflected by the stripe of heavy rainfall in the center of the forest strip in Figs. 8d and 8e.

These collision-initiated storms also produce intense cold pools associated with the evaporation of heavy precipitation along the center of the forest stripe. By 1600 LT, the average 15 m AGL air temperature over the forest has decreased to ~302.8 K in the PF simulation (Fig. 13b) and ~302.0 K in the SF simulation, compared to ~307.6 K for both the pasture and suburbs in the PF and SF simulations, respectively (supplemental animations 3d,e). We should note that these decreased temperatures are restricted to $y > +100$ km. The vast majority of precipitation and associated cold pools occur north of $y = +100$ km over the forest (Figs. 8d,e). A couple of storms do form between $y = +75$ km and $y = +100$ km around 1330 LT (Figs. 5d,e), but mixing with the warm air advected by the southerly background wind, as well as the strong sensible heat flux and high roughness length of the forest, quickly erodes these southern cold pools (Gentine et al. 2016; Grant and van den Heever 2018). South of this line, where the development of convection is inhibited by

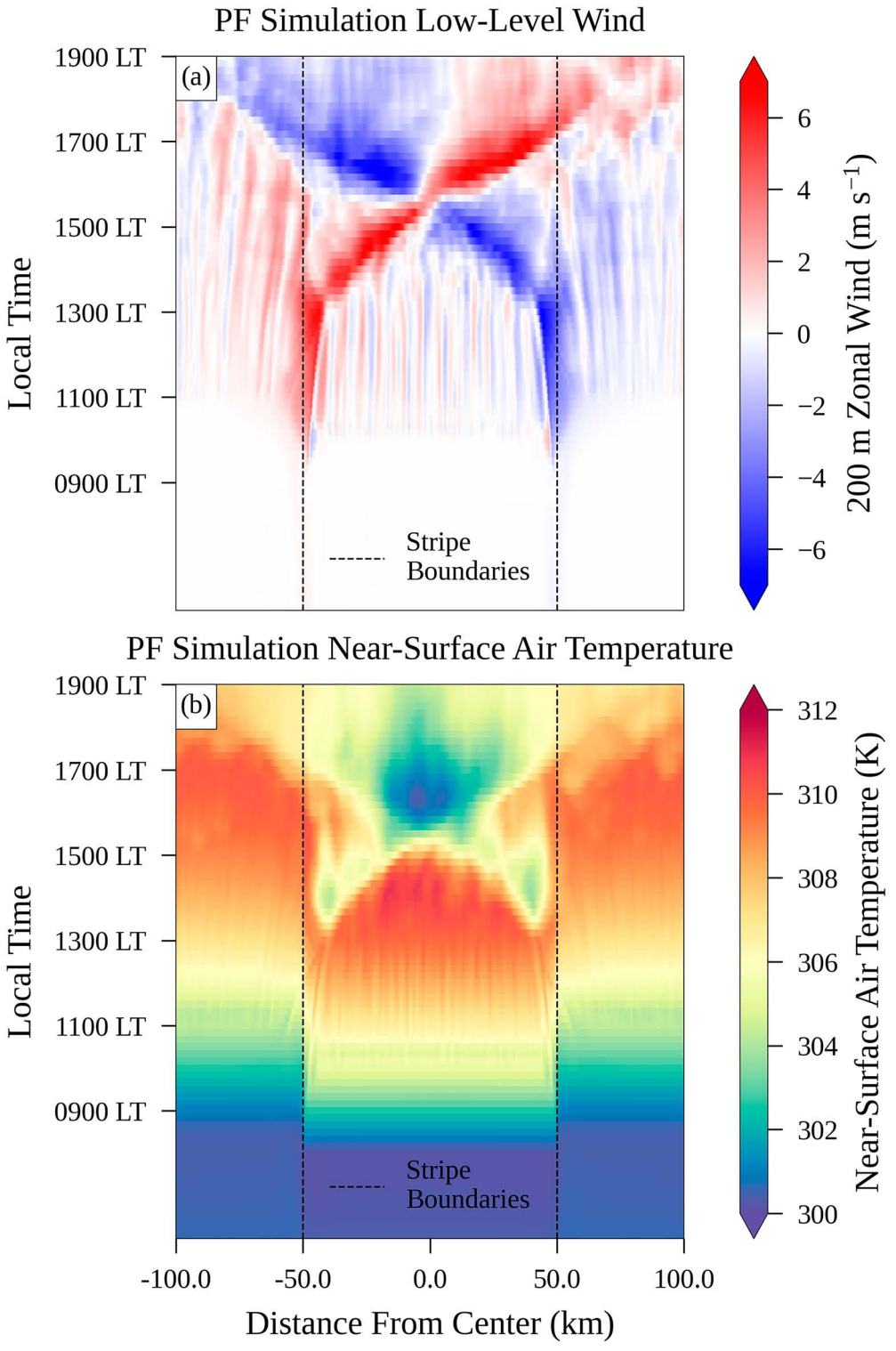

FIG. 13. Hovmöller diagrams of (a) 200-m zonal wind velocity and (b) 15-m air temperature in the PF simulation. Zonal winds and air temperatures are averaged over the y direction from $y = +100$ km to $y = +250$ km. Distance from the center of the forest stripe is shown on the horizontal axis, while time is displayed on the vertical axis.

stabilizing marine influence, the forest remains warmer than the surrounding pasture and suburbs (supplemental animations 3d,e). This leads to two distinct circulation patterns that are now present at each forest boundary. North of $y = +100$ km, the reduced temperatures over the forest produced by the strong cold pools have induced larger surface pressures there than the surrounding suburbs or pasture (approximately 1.2 hPa larger over the forest than pasture in the PF simulation and 1.3 hPa larger than the suburbs in the SF simulation) (supplemental animations 4d,e), which in turn leads to divergent near-surface flow over the forest after 1600 LT (Fig. 13a). This divergent flow advects cool, moist air from the forest over the pasture and suburbs. These findings are in line with those of Harvey et al. (2022), who noted that after deep convection had initiated and cold pools had been produced over the drier patches, inflow over the dry patches transitioned to outflow associated with the cold pools. South of $y = +100$ km, the temperatures over the forest remain greater than those over the pasture and suburbs, resulting in reduced surface pressure and continued near-surface inflow over the forest from the original forest breeze (supplemental animations 3d,e, 4d,e, and 5d,e).

The cold pool circulation and the residual forest breeze circulation intersect over the forest at $y = +100$ km, resulting in the initiation of new deep convection along this line after 1600 LT (supplemental animations 1d,e and 5d,e). Additionally, storms form over the pasture and suburbs in the PF and SF simulations, respectively, as the cold pool from the forest spreads outward.

In contrast to the PF and SF simulations, the differences between the SP simulation and the uniform land surface simulations are subtle. Indeed, this simulation behaves more similarly to the UP or US simulations than to the PF and SF simulations. The rainfall is concentrated over the suburbs, with a mean accumulated rainfall of ~0.729 mm compared with a mean accumulated rainfall over the pasture of ~0.464 mm (Fig. 8f). This is likely due to a slightly more favorable convective environment over the suburb than the pasture (Figs. 6f and 7f). These differences in the convective environment are a result of greater sensible and latent heating over the suburbs compared to the pasture. However, there are no clear solenoidal circulations which form on the boundaries of the pasture and suburbs, which means that deep convection initially develops along the sea-breeze front before developing inland, similarly to the UP and US simulations. This is reflected in Fig. 8f, in which precipitation is scattered more or less randomly throughout each land surface type, with only a weak gradient in precipitation between the pasture and suburbs.

4. Discussion and conclusions

To examine the role of vegetation heterogeneity and the sea breeze in convection initiation and development, we ran six idealized simulations of convection in a coastal environment. Three of these simulations (UP, UF, and US) employed a uniform vegetation type, while three simulations (PF, SF, and SP) contained two stripes of different vegetation types.

The results of this research indicate that the presence of sharp heterogeneities in vegetation type enhances the development of convective storms and precipitation. This enhancement occurs due to the presence of solenoidal circulations which arise from differences in PBL structure induced by differing adjacent vegetation types. In our PF and SF simulations, the near-surface air temperature over the forest, as a result of its greater vegetation fraction and roughness length, becomes greater than that over the surrounding pasture and suburbs. This greater near-surface temperature decreases surface pressure and produces higher PBL height over the forest than over its surroundings. This difference in pressure and PBL height induces a forest breeze: a solenoidal circulation with near-surface inflow and rising over the forest and sinking motion over the pasture/suburbs (Fig. 12). Figure 14a presents a schematic which illustrates how the converging and rising branches of the forest breeze initiate convective storms over the edges of the forest, while the downward branches of the forest breeze suppress precipitation over the surrounding pasture.

These findings, indicating that sensible heat fluxes are greater over coniferous forests compared to adjacent suburbs and pasture, do seem counterintuitive at first glance. However, we should emphasize that initial soil moisture was very limited in these simulations, which reflected drought conditions observed in Houston in June 2022 during the ESCAPE and TRACER campaigns. This limited soil moisture prevents nearly all transpiration. Previous studies have also indicated that, especially under dry soil conditions, coniferous forests can have large sensible heat fluxes and Bowen ratios, in some cases greater than those of adjacent pasture and agricultural lands (Beyrich et al. 2006; Lee and Black 1993; Lundin et al. 1999; Mahrt and Ek 1993; Mascart et al. 1991; Starkenburg et al. 2015).

The rising branches of the forest breeze appear to be more important than the sea breeze in determining the location and timing of convection initiation in the PF and SF simulations. Unlike in the uniform land surface simulations, in which strong convection is initially limited to being along the sea-breeze front, in simulations PF and SF strong convection also initiates along the forest boundary, and not just along the sea-breeze front.

The first storms initiated along the forest boundary, driven by the rising branches of the forest breeze, produce precipitation which evaporates near the surface to produce cold pools (Fig. 14a). These cold pools spread inward toward the center of the forest, propagating the pattern of near-surface inflow over the forest inward toward the center of the forest stripe (Figs. 13a and 14b). As the two sides of the inflow collide along the center of the forest, they initiate intense convective storms as a result of strong mechanical lifting. These convective storms then produce heavy precipitation along the center of the forest stripe (Figs. 8d,e and 14c). The propagation speed of the inflow branches prior to the development of cold pools suggests that they may not have collided in the center of the forest stripe without reinforcement from cold pools. The intensity of the collision-initiated storms in the center of the forest stripe, and the role of cold pools in that collision, also suggests that the interaction of cold pools with the forest breeze enhances convection initiation. At the same time, it appears that cold pools are primarily responsible for the destruction of the forest breeze later in the day. The forest

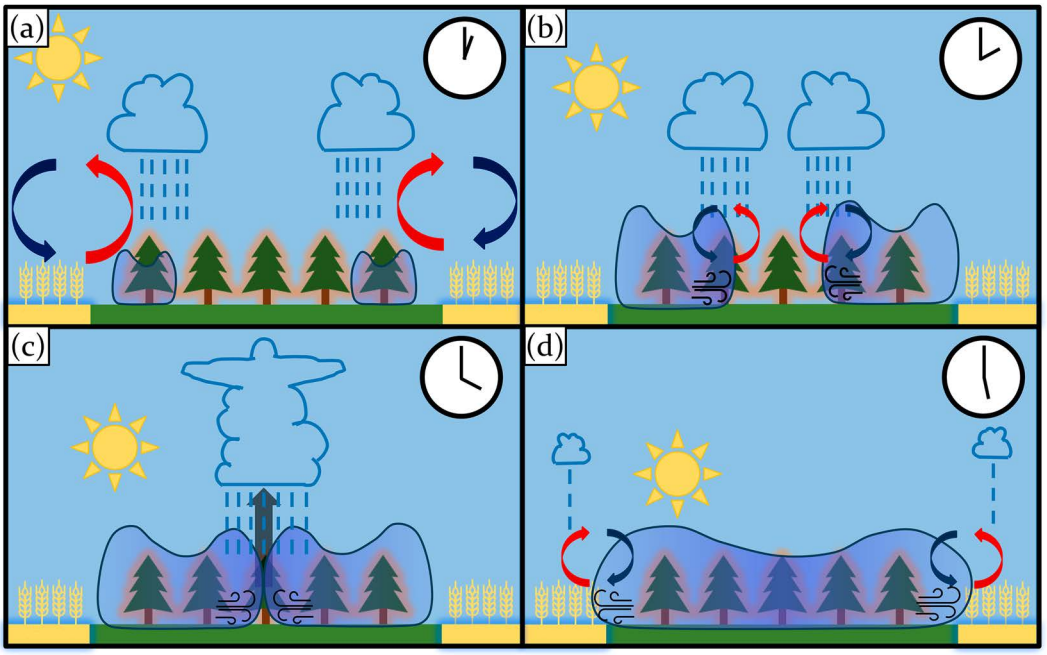

FIG. 14. Cartoon schematic of the evolution of the forest breeze, cold pools, and convection in the PF simulation. Solenoidal circulations are in red and blue arrows, cold pools are in blue shading, and wind gusts at the edge of cold pools are in black curves. The collision of the cold pools in the center of the forest stripe in (c) results in the formation of strong convection with heavy rainfall. (a) 1230, (b) 1400, (c) 1600, and (d) 1730 LT.

becomes colder than the surrounding pasture and suburbs after 1600 LT, leading to larger surface pressure over the forest and near-surface divergence from the forest to the pasture and suburbs (Figs. 13a,b and 14d).

We should also add that these forest breezes and the storms they initiate are sensitive to the size of the vegetation stripes. In our simulations, the rising branches of the two forest breeze circulations were approximately 15 km from the center of the circulation as seen in Fig. 12, implying an "ideal forest stripe size" of approximately 30 km. However, even if this "ideal strip size" promoted the development of stronger storms earlier in the day by allowing the forest breezes to collide earlier, this would not necessarily increase total precipitation over the forest. The storms initiating in the middle of the forest stripe would quickly precipitate and produce intense cold pools as occur in the PF and SF simulations after 1600 LT (supplemental animations 3d,e). Once this happened, instability over the forest would decrease and storms would quickly weaken and die out. Over our 100-km-wide forest stripe, by contrast, storms can start on the edge and progress inward following cold pools. This allows convection to continue for many hours over the forest as storms continually have access to CAPE. This suggests that the existence of cold pools may change which stripe size leads to the most precipitation over the hotter vegetation type.

The interactions of forest breezes, cold pools, and sea breezes and their impacts on coastal convection are complex and not completely understood. Future study of these phenomena, and their interaction with other factors such as topography and urban effects, may improve our understanding and subsequent forecasting of the location, timing, and hazards of convective storms in the coastal environment.

Acknowledgments. The authors thank Dr. Aryeh Drager, Dr. Leah Grant, Dr. Ian Baker, and Dr. Hassan Dashtian for their assistance with this research. We would also like to thank the editors and peer reviewers at the Journal of Atmospheric Sciences for volunteering their time to read and review this manuscript. Their feedback has been extremely helpful in improving this paper. This research was supported by the NSF Grant AGS-2019947. S.C. van den Heever and S.M. Saleeby also acknowledge funding from DOE Grant DE-SC0021160. This work is supported by INCUS, a NASA Earth Venture Mission, funded by NASA's Science Mission Directorate and managed through the Earth System Science Pathfinder Program Office under Contract 80LARC22DA011. P.J. Marinescu acknowledges funding from INCUS.

Data availability statement. While the analysis and post-processed datasets used for this analysis are too large to easily share, the data can be recreated by following the instructions and using files which are located on Zenodo at the following doi: https://doi.org/10.5281/zenodo.13697467.

REFERENCES

Allouche, M., E. Bou-Zeid, and J. Iipponen, 2023: The influence of synoptic wind on land–sea breezes. *Quart. J. Roy. Meteor. Soc.*, **149**, 3198–3219, https://doi.org/10.1002/qj.4552.

Anthes, R. A., 1978: The height of the planetary boundary layer and the production of circulation in a sea breeze model. *J. Atmos. Sci.*, **35**, 1231–1239, https://doi.org/10.1175/1520-0469(1978)035<1231:THOTPB>2.0.CO;2.

——, 1984: Enhancement of convective precipitation by mesoscale variations in vegetative covering in semiarid regions. *J. Climate Appl. Meteor.*, **23**, 541–554, https://doi.org/10.1175/1520-0450(1984)023<0541:EOCPBM>2.0.CO;2.

Antonelli, M., and R. Rotunno, 2007: Large-eddy simulation of the onset of the sea breeze. *J. Atmos. Sci.*, **64**, 4445–4457, https://doi.org/10.1175/2007JAS2261.1.

Arakawa, A., and V. R. Lamb, 1977: Computational design of the basic dynamical processes of the UCLA general circulation model. *Methods in Computational Physics: Advances in Research and Applications*, J. Chang, Ed., General Circulation Models of the Atmosphere, Vol. 17, Elsevier, 173–265, https://doi.org/10.1016/B978-0-12-460817-7.50009-4.

Avissar, R., and Y. Liu, 1996: Three-dimensional numerical study of shallow convective clouds and precipitation induced by land surface forcing. *J. Geophys. Res.*, **101**, 7499–7518, https://doi.org/10.1029/95JD03031.

Beyrich, F., and Coauthors, 2006: Area-averaged surface fluxes over the Litfass region based on eddy-covariance measurements. *Bound.-Layer Meteor.*, **121**, 33–65, https://doi.org/10.1007/s10546-006-9052-x.

Bou-Zeid, E., W. Anderson, G. G. Katul, and L. Mahrt, 2020: The persistent challenge of surface heterogeneity in boundary-layer meteorology: A review. *Bound.-Layer Meteor.*, **177**, 227–245, https://doi.org/10.1007/s10546-020-00551-8.

Branch, O., and V. Wulfmeyer, 2019: Deliberate enhancement of rainfall using desert plantations. *Proc. Natl. Acad. Sci. USA*, **116**, 18 841–18 847, https://doi.org/10.1073/pnas.1904754116.

Brown, M. E., and D. L. Arnold, 1998: Land-surface–atmosphere interactions associated with deep convection in Illinois. *Int. J. Climatol.*, **18**, 1637–1653, https://doi.org/10.1002/(SICI)1097-0088(199812)18:15<1637::AID-JOC336>3.0.CO;2-U.

Chagnon, F. J. F., R. L. Bras, and J. Wang, 2004: Climatic shift in patterns of shallow clouds over the Amazon. *Geophys. Res. Lett.*, **31**, L24212, https://doi.org/10.1029/2004GL021188.

Chen, F., and R. Avissar, 1994: Impact of land-surface moisture variability on local shallow convective cumulus and precipitation in large-scale models. *J. Appl. Meteor.*, **33**, 1382–1401, https://doi.org/10.1175/1520-0450(1994)033<1382:IOLSMV>2.0.CO;2.

Chen, J., S. Hagos, H. Xiao, J. D. Fast, and Z. Feng, 2020: Characterization of surface heterogeneity-induced convection using cluster analysis. *J. Geophys. Res. Atmos.*, **125**, e2020JD032550, https://doi.org/10.1029/2020JD032550.

Cheng, W. Y. Y., and W. R. Cotton, 2004: Sensitivity of a cloud-resolving simulation of the genesis of a mesoscale convective system to horizontal heterogeneities in soil moisture initialization. *J. Hydrometeor.*, **5**, 934–958, https://doi.org/10.1175/1525-7541(2004)005<0934:SOACSO>2.0.CO;2.

Cheng, Y., and K. A. McColl, 2023: Thermally direct mesoscale circulations caused by land surface roughness anomalies. *Geophys. Res. Lett.*, **50**, e2023GL105150, https://doi.org/10.1029/2023GL105150.

——, P. W. Chan, X. Wei, Z. Hu, Z. Kuang, and K. A. McColl, 2021: Soil moisture control of precipitation reevaporation over a heterogeneous land surface. *J. Atmos. Sci.*, **78**, 3369–3383, https://doi.org/10.1175/JAS-D-21-0059.1.

——, Z. Hu, and K. A. McColl, 2023: Anomalously darker land surfaces become wetter due to mesoscale circulations. *Geophys. Res. Lett.*, **50**, e2023GL104137, https://doi.org/10.1029/2023GL104137.

Cioni, G., and C. Hohenegger, 2018: A simplified model of precipitation enhancement over a heterogeneous surface. *Hydrol. Earth Syst. Sci.*, **22**, 3197–3212, https://doi.org/10.5194/hess-22-3197-2018.

Cotton, W. R., and Coauthors, 2003: RAMS 2001: Current status and future directions. *Meteor. Atmos. Phys.*, **82**, 5–29, https://doi.org/10.1007/s00703-001-0584-9.

Dashtian, H., and M. H. Young, 2023: Soil water content and meteorological data to support Tracking Aerosol Convection Interactions ExpeRiment (TRACER) over Harris county, Texas. Texas Data Repository, accessed 2 March 2023, https://doi.org/10.18738/T8/FN3RWZ.

Derbyshire, S. H., I. Beau, P. Bechtold, J.-Y. Grandpeix, J.-M. Piriou, J.-L. Redelsperger, and P. M. M. Soares, 2004: Sensitivity of moist convection to environmental humidity. *Quart. J. Roy. Meteor. Soc.*, **130**, 3055–3079, https://doi.org/10.1256/qj.03.130.

DeWitz, J., and USGS, 2021: National Land Cover Database (NLCD) 2019 products (ver. 3.0, February 2024). US Geological Survey data release, accessed 19 July 2024, https://doi.org/10.5066/P9KZCM54.

Drager, A. J., L. D. Grant, and S. C. van den Heever, 2022: A nonmonotonic precipitation response to changes in soil moisture in the presence of vegetation. *J. Hydrometeor.*, **23**, 1095–1111, https://doi.org/10.1175/JHM-D-21-0109.1.

Emori, S., 1998: The interaction of cumulus convection with soil moisture distribution: An idealized simulation. *J. Geophys. Res.*, **103**, 8873–8884, https://doi.org/10.1029/98JD00426.

Esau, I. N., and T. J. Lyons, 2002: Effect of sharp vegetation boundary on the convective atmospheric boundary layer. *Agric. For. Meteor.*, **114**, 3–13, https://doi.org/10.1016/S0168-1923(02)00154-5.

Fast, J. D., L. K. Berg, Z. Feng, F. Mei, R. Newsom, K. Sakaguchi, and H. Xiao, 2019: The impact of variable land-atmosphere coupling on convective cloud populations observed during the 2016 HI-SCALE field campaign. *J. Adv. Model. Earth Syst.*, **11**, 2629–2654, https://doi.org/10.1029/2019MS001727.

Fogarty, J., and E. Bou-Zeid, 2023: The atmospheric boundary layer above the marginal ice zone: Scaling, surface fluxes, and secondary circulations. *Bound.-Layer Meteor.*, **189**, 53–76, https://doi.org/10.1007/s10546-023-00825-x.

Garcia-Carreras, L., D. J. Parker, and J. H. Marsham, 2011: What is the mechanism for the modification of convective cloud distributions by land surface–induced flows? *J. Atmos. Sci.*, **68**, 619–634, https://doi.org/10.1175/2010JAS3604.1.

Gentine, P., A. Garelli, S.-B. Park, J. Nie, G. Torri, and Z. Kuang, 2016: Role of surface heat fluxes underneath cold pools. *Geophys. Res. Lett.*, **43**, 874–883, https://doi.org/10.1002/2015GL067262.

Giorgi, F., and R. Avissar, 1997: Representation of heterogeneity effects in Earth system modeling: Experience from land surface modeling. *Rev. Geophys.*, **35**, 413–437, https://doi.org/10.1029/97RG01754.

Grant, L. D., and S. C. van den Heever, 2014: Aerosol-cloud-land surface interactions within tropical sea breeze convection. *J. Geophys. Res. Atmos.*, **119**, 8340–8361, https://doi.org/10.1002/2014JD021912.

——, and ——, 2018: Cold pool-land surface interactions in a dry continental environment. *J. Adv. Model. Earth Syst.*, **10**, 1513–1526, https://doi.org/10.1029/2018MS001323.

Harrington, J. Y., 1997: The effects of radiative and microphysical processes on simulated warm and transition season arctic stratus. Ph.D. thesis, Dept. of Atmospheric Science, Colorado State University, 289 pp., https://ui.adsabs.harvard.edu/abs/1997PhDT.....45H/abstract.

Harvey, N. J., C. L. Daleu, R. A. Stratton, R. S. Plant, S. J. Woolnough, and A. J. Stirling, 2022: The impact of surface heterogeneity on the diurnal cycle of deep convection. *Quart. J. Roy. Meteor. Soc.*, **148**, 3509–3527, https://doi.org/10.1002/qj.4371.

Hill, G. E., 1974: Factors controlling the size and spacing of cumulus clouds as revealed by numerical experiments. *J. Atmos. Sci.*, **31**, 646–673, https://doi.org/10.1175/1520-0469(1974)031<0646:FCTSAS>2.0.CO;2.

Hong, X., M. J. Leach, and S. Raman, 1995: A sensitivity study of convective cloud formation by vegetation forcing with different atmospheric conditions. *J. Appl. Meteor.*, **34**, 2008–2028, https://doi.org/10.1175/1520-0450(1995)034<2008:ASSOCC>2.0.CO;2.

Igel, A. L., S. C. van den Heever, and J. S. Johnson, 2018: Meteorological and land surface properties impacting sea breeze extent and aerosol distribution in a dry environment. *J. Geophys. Res. Atmos.*, **123**, 22–37, https://doi.org/10.1002/2017JD027339.

Jensen, M., and Coauthors, 2023: Tracking Aerosol Convection Interactions Experiment (TRACER) field campaign report. Department of Energy, Field Campaign Tech. Rep. DOE/SC-ARM-23-038, 132 pp., https://doi.org/10.2172/2202672.

Kang, S.-L., and G. H. Bryan, 2011: A large-eddy simulation study of moist convection initiation over heterogeneous surface fluxes. *Mon. Wea. Rev.*, **139**, 2901–2917, https://doi.org/10.1175/MWR-D-10-05037.1.

Kawase, H., T. Yoshikane, M. Hara, F. Kimura, T. Sato, and S. Ohsawa, 2008: Impact of extensive irrigation on the formation of cumulus clouds. *Geophys. Res. Lett.*, **35**, L01806, https://doi.org/10.1029/2007GL032435.

Keeler, E., K. Burk, and J. Kyrouac, 2022: Balloon-Borne Sounding System (sondewnpn): Vaisala-processed winds, press., temp, & RH. ARM, accessed 14 February 2023, https://doi.org/10.5439/1595321.

Klemp, J. B., and R. B. Wilhelmson, 1978: The simulation of three-dimensional convective storm dynamics. *J. Atmos. Sci.*, **35**, 1070–1096, https://doi.org/10.1175/1520-0469(1978)035<1070:TSOTDC>2.0.CO;2.

Kollias, P., and Coauthors, 2024: Experiment of Sea Breeze Convection, Aerosols, Precipitation and Environment (ESCAPE). *Bull. Amer. Meteor. Soc.*, https://doi.org/10.1175/BAMS-D-23-0014.1, in press.

Lee, J. M., Y. Zhang, and S. A. Klein, 2019: The effect of land surface heterogeneity and background wind on shallow cumulus clouds and the transition to deeper convection. *J. Atmos. Sci.*, **76**, 401–419, https://doi.org/10.1175/JAS-D-18-0196.1.

Lee, S.-H., and F. Kimura, 2001: Comparative studies in the local circulations induced by land-use and by topography. *Bound.-Layer Meteor.*, **101**, 157–182, https://doi.org/10.1023/A:1019219412907.

Lee, X., and T. A. Black, 1993: Atmospheric turbulence within and above a douglas-fir stand. Part II: Eddy fluxes of sensible heat and water vapour. *Bound.-Layer Meteor.*, **64**, 369–389, https://doi.org/10.1007/BF00711706.

Lilly, D. K., 1962: On the numerical simulation of buoyant convection. *Tellus*, **14**, 148–172, https://doi.org/10.3402/tellusa.v14i2.9537.

Lundin, L.-C., and Coauthors, 1999: Continuous long-term measurements of soil-plant-atmosphere variables at a forest site. *Agric. For. Meteor.*, **98–99**, 53–73, https://doi.org/10.1016/S0168-1923(99)00092-1.

Lynn, B. H., W.-K. Tao, and P. J. Wetzel, 1998: A study of landscape-generated deep moist convection. *Mon. Wea. Rev.*, **126**, 928–942, https://doi.org/10.1175/1520-0493(1998)126<0928:ASOLGD>2.0.CO;2.

Mahrt, L., and M. Ek, 1993: Spatial variability of turbulent fluxes and roughness lengths in HAPEX-MOBILHY. *Bound.-Layer Meteor.*, **65**, 381–400, https://doi.org/10.1007/BF00707034.

Mascart, P., O. Taconet, J.-P. Pinty, and M. B. Mehrez, 1991: Canopy resistance formulation and its effect in mesoscale models: A HAPEX perspective. *Agric. For. Meteor.*, **54**, 319–351, https://doi.org/10.1016/0168-1923(91)90012-F.

Nair, U. S., Y. Wu, J. Kala, T. J. Lyons, R. A. Pielke Sr., and J. M. Hacker, 2011: The role of land use change on the development and evolution of the west coast trough, convective clouds, and precipitation in southwest Australia. *J. Geophys. Res.*, **116**, D07103, https://doi.org/10.1029/2010JD014950.

Ookouchi, Y., M. Segal, R. C. Kessler, and R. A. Pielke, 1984: Evaluation of soil moisture effects on the generation and modification of mesoscale circulations. *Mon. Wea. Rev.*, **112**, 2281–2292, https://doi.org/10.1175/1520-0493(1984)112<2281:EOSMEO>2.0.CO;2.

Park, J. M., S. C. van den Heever, A. L. Igel, L. D. Grant, J. S. Johnson, S. M. Saleeby, S. D. Miller, and J. S. Reid, 2020: Environmental controls on tropical sea breeze convection and resulting aerosol redistribution. *J. Geophys. Res. Atmos.*, **125**, e2019JD031699, https://doi.org/10.1029/2019JD031699.

Patton, E. G., P. P. Sullivan, and C.-H. Moeng, 2005: The influence of idealized heterogeneity on wet and dry planetary boundary layers coupled to the land surface. *J. Atmos. Sci.*, **62**, 2078–2097, https://doi.org/10.1175/JAS3465.1.

Phillips, C. E., U. S. Nair, R. Mahmood, E. Rappin, and R. A. Pielke Sr., 2022: Influence of irrigation on diurnal mesoscale circulations: Results from GRAINEX. *Geophys. Res. Lett.*, **49**, e2021GL096822, https://doi.org/10.1029/2021GL096822.

Pinty, J.-P., P. Mascart, E. Richard, and R. Rosset, 1989: An investigation of mesoscale flows induced by vegetation inhomogeneities using an evapotranspiration model calibrated against HAPEX-MOBILHY data. *J. Appl. Meteor.*, **28**, 976–992, https://doi.org/10.1175/1520-0450(1989)028<0976:AIOMFI>2.0.CO;2.

Rabin, R. M., S. Stadler, P. J. Wetzel, D. J. Stensrud, and M. Gregory, 1990: Observed effects of landscape variability on convective clouds. *Bull. Amer. Meteor. Soc.*, **71**, 272–280, https://doi.org/10.1175/1520-0477(1990)071<0272:OEOLVO>2.0.CO;2.

Rapp, A. D., C. D. Kummerow, and L. Fowler, 2011: Interactions between warm rain clouds and atmospheric preconditioning for deep convection in the tropics. *J. Geophys. Res.*, **116**, D23210, https://doi.org/10.1029/2011JD016143.

Reynolds, R. W., N. A. Rayner, T. M. Smith, D. C. Stokes, and W. Wang, 2002: An improved in situ and satellite SST analysis for climate. *J. Climate*, **15**, 1609–1625, https://doi.org/10.1175/1520-0442(2002)015<1609:AIISAS>2.0.CO;2.

Rieck, M., C. Hohenegger, and C. C. van Heerwaarden, 2014: The influence of land surface heterogeneities on cloud size development. *Mon. Wea. Rev.*, **142**, 3830–3846, https://doi.org/10.1175/MWR-D-13-00354.1.

——, ——, and P. Gentine, 2015: The effect of moist convection on thermally induced mesoscale circulations. *Quart. J. Roy. Meteor. Soc.*, **141**, 2418–2428, https://doi.org/10.1002/qj.2532.

Saleeby, S. M., and W. R. Cotton, 2004: A large-droplet mode and prognostic number concentration of cloud droplets in the Colorado State University Regional Atmospheric Modeling System (RAMS). Part I: Module descriptions and supercell test simulations. *J. Appl. Meteor.*, **43**, 182–195, https://doi.org/10.1175/1520-0450(2004)043<0182:ALMAPN>2.0.CO;2.

——, and S. C. van den Heever, 2013: Developments in the CSU-RAMS aerosol model: Emissions, nucleation, regeneration, deposition, and radiation. *J. Appl. Meteor. Climatol.*, **52**, 2601–2622, https://doi.org/10.1175/JAMC-D-12-0312.1.

Sato, T., F. Kimura, and A. S. Hasegawa, 2007: Vegetation and topographic control of cloud activity over arid/semiarid Asia. *J. Geophys. Res.*, **112**, D24109, https://doi.org/10.1029/2006JD008129.

Segal, M., R. W. Arritt, C. Clark, R. Rabin, and J. Brown, 1995: Scaling evaluation of the effect of surface characteristics on potential for deep convection over uniform terrain. *Mon. Wea. Rev.*, **123**, 383–400, https://doi.org/10.1175/1520-0493(1995)123<0383:SEOTEO>2.0.CO;2.

Simpson, J. E., 1996: Diurnal changes in sea-breeze direction. *J. Appl. Meteor.*, **35**, 1166–1169, https://doi.org/10.1175/1520-0450(1996)035%3C1166:DCISBD%3E2.0.CO;2.

Smagorinsky, J., 1963: General circulation experiments with the primitive equations 1: The basic experiment. *Mon. Wea. Rev.*, **91**, 99–164, https://doi.org/10.1175/1520-0493(1963)091<0099:GCEWTP>2.3.CO;2.

Starkenburg, D., and Coauthors, 2015: Temperature regimes and turbulent heat fluxes across a heterogeneous canopy in an Alaskan boreal forest. *J. Geophys. Res. Atmos.*, **120**, 1348–1360, https://doi.org/10.1002/2014JD022338.

Sykes, R. I., W. S. Lewellen, and D. S. Henn, 1988: A numerical study of the development of Claud-street spacing. *J. Atmos. Sci.*, **45**, 2556–2570, https://doi.org/10.1175/1520-0469(1988)045<2556:ANSOTD>2.0.CO;2.

Taylor, C. M., R. A. M. de Jeu, F. Guichard, P. P. Harris, and W. A. Dorigo, 2012: Afternoon rain more likely over drier soils. *Nature*, **489**, 423–426, https://doi.org/10.1038/nature11377.

Teuling, A. J., and Coauthors, 2017: Observational evidence for cloud cover enhancement over western European forests. *Nat. Commun.*, **8**, 14065, https://doi.org/10.1038/ncomms14065.

Walko, R. L., and Coauthors, 2000: Coupled atmosphere–biophysics–hydrology models for environmental modeling. *J. Appl. Meteor.*, **39**, 931–944, https://doi.org/10.1175/1520-0450(2000)039<0931:CABHMF>2.0.CO;2.

Wang, C., W. Tian, D. J. Parker, J. H. Marsham, and Z. Guo, 2011: Properties of a simulated convective boundary layer over inhomogeneous vegetation. *Quart. J. Roy. Meteor. Soc.*, **137**, 99–117, https://doi.org/10.1002/qj.724.

Weckwerth, T. M., J. W. Wilson, and R. M. Wakimoto, 1996: Thermodynamic variability within the convective boundary layer due to horizontal convective rolls. *Mon. Wea. Rev.*, **124**, 769–784, https://doi.org/10.1175/1520-0493(1996)124<0769:TVWTCB>2.0.CO;2.

Weisman, M. L., and J. B. Klemp, 1984: The structure and classification of numerically simulated convective stormsin directionally varying wind shears. *Mon. Wea. Rev.*, **112**, 2479–2498, https://doi.org/10.1175/1520-0493(1984)112<2479:TSACON>2.0.CO;2.

Yan, H., and R. A. Anthes, 1987: The effect of latitude on the sea breeze. *Mon. Wea. Rev.*, **115**, 936–956, https://doi.org/10.1175/1520-0493(1987)115<0936:TEOLOT>2.0.CO;2.